Multi-Differential Cross Section Measurements of ν_μ-Argon Quasielastic-like Reactions with the MicroBooNE Detector

P. Abratenko,[35] O. Alterkait,[35] D. Andrade Aldana,[15] J. Anthony,[5] L. Arellano,[20] J. Asaadi,[34] A. Ashkenazi,[32] S. Balasubramanian,[12] B. Baller,[12] G. Barr,[25] J. Barrow,[21,32] V. Basque,[12] O. Benevides Rodrigues,[31] S. Berkman,[12] A. Bhanderi,[20] M. Bhattacharya,[12] M. Bishai,[3] A. Blake,[17] B. Bogart,[22] T. Bolton,[16] J. Y. Book,[14] L. Camilleri,[10] D. Caratelli,[4] I. Caro Terrazas,[9] F. Cavanna,[12] G. Cerati,[12] Y. Chen,[28] J. M. Conrad,[21] M. Convery,[28] L. Cooper-Troendle,[39] J. I. Crespo-Anadón,[6] M. Del Tutto,[12] S. R. Dennis,[5] P. Detje,[5] A. Devitt,[17] R. Diurba,[2] Z. Djurcic,[1] R. Dorrill,[15] K. Duffy,[25] S. Dytman,[26] B. Eberly,[30] A. Ereditato,[2] J. J. Evans,[20] R. Fine,[18] O. G. Finnerud,[20] W. Foreman,[15] B. T. Fleming,[39] N. Foppiani,[14] D. Franco,[39] A. P. Furmanski,[23] D. Garcia-Gamez,[13] S. Gardiner,[12] G. Ge,[10] S. Gollapinni,[33,18] O. Goodwin,[20] E. Gramellini,[12] P. Green,[20,25] H. Greenlee,[12] W. Gu,[3] R. Guenette,[20] P. Guzowski,[20] L. Hagaman,[39] O. Hen,[21] R. Hicks,[18] C. Hilgenberg,[23] G. A. Horton-Smith,[16] B. Irwin,[23] R. Itay,[28] C. James,[12] X. Ji,[3] L. Jiang,[37] J. H. Jo,[3,39] R. A. Johnson,[8] Y.-J. Jwa,[10] D. Kalra,[10] N. Kamp,[21] G. Karagiorgi,[10] W. Ketchum,[12] M. Kirby,[12] T. Kobilarcik,[12] I. Kreslo,[2] M. B. Leibovitch,[4] I. Lepetic,[27] J.-Y. Li,[11] K. Li,[39] Y. Li,[3] K. Lin,[27] B. R. Littlejohn,[15] W. C. Louis,[18] X. Luo,[4] C. Mariani,[37] D. Marsden,[20] J. Marshall,[38] N. Martinez,[16] D. A. Martinez Caicedo,[29] K. Mason,[35] A. Mastbaum,[27] N. McConkey,[20,36] V. Meddage,[16] K. Miller,[7] J. Mills,[35] A. Mogan,[9] T. Mohayai,[12] M. Mooney,[9] A. F. Moor,[5] C. D. Moore,[12] L. Mora Lepin,[20] J. Mousseau,[22] S. Mulleriababu,[2] D. Naples,[26] A. Navrer-Agasson,[20] N. Nayak,[3] M. Nebot-Guinot,[11] J. Nowak,[17] N. Oza,[10,18] O. Palamara,[12] N. Pallat,[23] V. Paolone,[26] A. Papadopoulou,[1,21] V. Papavassiliou,[24] H. B. Parkinson,[11] S. F. Pate,[24] N. Patel,[17] Z. Pavlovic,[12] E. Piasetzky,[32] I. D. Ponce-Pinto,[39] I. Pophale,[17] S. Prince,[14] X. Qian,[3] J. L. Raaf,[12] V. Radeka,[3] A. Rafique,[1] M. Reggiani-Guzzo,[20] L. Ren,[24] L. Rochester,[28] J. Rodriguez Rondon,[29] M. Rosenberg,[35] M. Ross-Lonergan,[18] C. Rudolf von Rohr,[2] G. Scanavini,[39] D. W. Schmitz,[7] A. Schukraft,[12] W. Seligman,[10] M. H. Shaevitz,[10] R. Sharankova,[12] J. Shi,[5] E. L. Snider,[12] M. Soderberg,[31] S. Söldner-Rembold,[20] J. Spitz,[22] M. Stancari,[12] J. St. John,[12] T. Strauss,[12] S. Sword-Fehlberg,[24] A. M. Szelc,[11] W. Tang,[33] N. Taniuchi,[5] K. Terao,[28] C. Thorpe,[17] D. Torbunov,[3] D. Totani,[4] M. Toups,[12] Y.-T. Tsai,[28] J. Tyler,[16] M. A. Uchida,[5] T. Usher,[28] B. Viren,[3] M. Weber,[2] H. Wei,[19] A. J. White,[39] Z. Williams,[34] S. Wolbers,[12] T. Wongjirad,[35] M. Wospakrik,[12] K. Wresilo,[5] N. Wright,[21] W. Wu,[12] E. Yandel,[4] T. Yang,[12] L. E. Yates,[12] H. W. Yu,[3] G. P. Zeller,[12] J. Zennamo,[12] and C. Zhang[3]

(The MicroBooNE Collaboration)*

[1] *Argonne National Laboratory (ANL), Lemont, IL, 60439, USA*
[2] *Universität Bern, Bern CH-3012, Switzerland*
[3] *Brookhaven National Laboratory (BNL), Upton, NY, 11973, USA*
[4] *University of California, Santa Barbara, CA, 93106, USA*
[5] *University of Cambridge, Cambridge CB3 0HE, United Kingdom*
[6] *Centro de Investigaciones Energéticas, Medioambientales y Tecnológicas (CIEMAT), Madrid E-28040, Spain*
[7] *University of Chicago, Chicago, IL, 60637, USA*
[8] *University of Cincinnati, Cincinnati, OH, 45221, USA*
[9] *Colorado State University, Fort Collins, CO, 80523, USA*
[10] *Columbia University, New York, NY, 10027, USA*
[11] *University of Edinburgh, Edinburgh EH9 3FD, United Kingdom*
[12] *Fermi National Accelerator Laboratory (FNAL), Batavia, IL 60510, USA*
[13] *Universidad de Granada, Granada E-18071, Spain*
[14] *Harvard University, Cambridge, MA 02138, USA*
[15] *Illinois Institute of Technology (IIT), Chicago, IL 60616, USA*
[16] *Kansas State University (KSU), Manhattan, KS, 66506, USA*
[17] *Lancaster University, Lancaster LA1 4YW, United Kingdom*
[18] *Los Alamos National Laboratory (LANL), Los Alamos, NM, 87545, USA*
[19] *Louisiana State University, Baton Rouge, LA, 70803, USA*
[20] *The University of Manchester, Manchester M13 9PL, United Kingdom*
[21] *Massachusetts Institute of Technology (MIT), Cambridge, MA, 02139, USA*
[22] *University of Michigan, Ann Arbor, MI, 48109, USA*
[23] *University of Minnesota, Minneapolis, MN, 55455, USA*
[24] *New Mexico State University (NMSU), Las Cruces, NM, 88003, USA*
[25] *University of Oxford, Oxford OX1 3RH, United Kingdom*
[26] *University of Pittsburgh, Pittsburgh, PA, 15260, USA*
[27] *Rutgers University, Piscataway, NJ, 08854, USA*
[28] *SLAC National Accelerator Laboratory, Menlo Park, CA, 94025, USA*
[29] *South Dakota School of Mines and Technology (SDSMT), Rapid City, SD, 57701, USA*

[30] University of Southern Maine, Portland, ME, 04104, USA
[31] Syracuse University, Syracuse, NY, 13244, USA
[32] Tel Aviv University, Tel Aviv, Israel, 69978
[33] University of Tennessee, Knoxville, TN, 37996, USA
[34] University of Texas, Arlington, TX, 76019, USA
[35] Tufts University, Medford, MA, 02155, USA
[36] University College London, London WC1E 6BT, United Kingdom
[37] Center for Neutrino Physics, Virginia Tech, Blacksburg, VA, 24061, USA
[38] University of Warwick, Coventry CV4 7AL, United Kingdom
[39] Wright Laboratory, Department of Physics, Yale University, New Haven, CT, 06520, USA
(Dated: January 9, 2023)

We report on a flux-integrated multi-differential measurement of charged-current muon neutrino scattering on argon with one muon and one proton in the final state using the Booster Neutrino Beam and MicroBooNE detector at Fermi National Accelerator Laboratory. The data are studied as a function of various kinematic imbalance variables and of a neutrino energy estimator, and are compared to a number of event generator predictions. We find that the measured cross sections in different phase-space regions are sensitive to nuclear effects. Our results provide precision data to test and improve the neutrino-nucleus interaction models needed to perform high-accuracy oscillation analyses. Specific regions of phase-space are identified where further model refinements are most needed.

I. INTRODUCTION

High-precision measurements of the neutrino mixing angles, mass differences, and charge-parity violating phase, and the search for physics beyond the Standard Model are the primary physics goals of many currently operating as well as next-generation neutrino experiments [1–6]. These measurements require reliable comparisons of measured and theoretically-expected neutrino interaction rates in the corresponding detectors. Thus, understanding the neutrino-nucleus scattering processes in detail is a prerequisite for these experiments to reach their discovery potential. A number of neutrino oscillation experiments employ liquid argon time projection chambers (LArTPCs) [3–5, 7–9] to detect the particles produced in neutrino interactions. The ultimate goal of these efforts is both to reconstruct the energy of the neutrino based on the kinematics of the outgoing particles and to enable few-percent-level modeling of neutrino-argon interaction rates [10]. Therefore, high-accuracy modeling of neutrino-argon interactions is of the utmost importance [11–13].

This work presents the first measurement of flux-integrated single- and double-differential cross sections for muon-neutrino-argon (ν_μ-Ar) charged-current (CC) quasielastic (QE)-like scattering reactions as a function of kinematic imbalance variables [14–18]. Double-differential measurements as a function of a neutrino energy estimator are further reported for the first time in kinematic imbalance bins on argon. Motivated by a previous analysis with a similar signal event topology [19], we focus on reactions where a single muon-proton pair is reconstructed with no additional detected particles. The results reported here use the MicroBooNE detector [20] with an exposure of 6.79×10^{20} protons on target from the Booster Neutrino Beam (BNB) [21] at Fermi National Accelerator Laboratory.

The experimental setup is presented in Sec. II, followed by the signal definition and event selection in Sec. III. The observables of interest are defined in Sec. IV. Section V describes the cross section extraction and systematics procedure and Sec. VI outlines the modeling configurations used for comparison to the data. The results are reported in Sec. VII and the conclusions are discussed in Sec. VIII.

II. EXPERIMENTAL SETUP

The MicroBooNE LArTPC has an active volume that contains 85 tonnes of argon. It is exposed to BNB neutrinos, with an energy spectrum that peaks around 0.8 GeV and extends to 2 GeV.

Charged particles are produced after the primary neutrino interaction with the argon nuclei in the LArTPC active volume. Scintillation light and electron ionization trails are produced while these charged particles travel through the liquid argon. In the presence of an electric field of 273 V/cm, the ionization electrons drift towards a system of three anode wire planes. Photomultiplier tubes (PMTs) are used to measure the scintillation light.

If the PMT signals are in time coincidence with the beam arrival time, then events are recorded. Trigger hardware and software selection criteria are designed to minimize the contribution from background events, which are primarily cosmic muons. After these are applied, enriched data samples are obtained in which a neutrino interaction occurs in $\approx 15\%$ of selected beam spills [22].

Individual particle tracks are reconstructed with `Pandora` pattern recognition algorithms based on the measured ionization signals in the enriched data sam-

* microboone_info@fnal.gov

ples [23]. Particles are identified based on the measured track energy deposition profile, while the particle momenta are obtained based on the track length [24, 25].

III. SIGNAL DEFINITION & EVENT SELECTION

The QE-like signal definition used in this analysis includes all ν_μ-Ar scattering events with a final-state muon with momentum $0.1 < p_\mu < 1.2\,\mathrm{GeV}/c$, and exactly one proton with $0.3 < p_p < 1\,\mathrm{GeV}/c$. Events with final-state neutral pions at any momentum are excluded. Signal events may contain any number of protons below 300 MeV/c or above $1\,\mathrm{GeV}/c$, neutrons at any momentum, and charged pions with momentum lower than 70 MeV/c. We refer to the events passing this definition as CC1p0π. This signal consists predominantly of QE events. More complex interactions, namely meson exchange currents (MEC), resonance interactions (RES) and deep inelastic scattering events (DIS), can mimic the experimental signature of true QE events due to final-state interactions (FSI) or particles not satisfying the signal definition as defined above.

Candidate muon-proton pairs are isolated by requiring the existence of precisely two track-like and no shower-like objects, as classified by `Pandora` using a track-score variable [26, 27]. The log-likelihood ratio (LLR) particle identification (PID) score [28] is used to identify the muon and proton candidates. Muons tend to have higher LLR PID score values than protons, thus the track with the highest score is tagged as the candidate muon. Meanwhile, the track with the lower score is treated as the candidate proton.

Cosmic muon and non-CC1p0π contamination backgrounds were significantly reduced by applying a requirement on the candidate proton LLR PID score. We studied the effect of cutting on different values of this quantity, which has a strong discrimination power for rejecting MC non-CC1p0π background, out-of-cryostat and cosmic events. That yielded an optimal cut on the proton candidate LLR score of < 0.05. To further minimize the contribution of mis-reconstructed track directions, we took advantage of two muon momentum reconstruction methods available for contained tracks, namely the momentum from range [29] and the momentum from Multiple Coulomb Scattering (MCS) [30]. The range and MCS muon momenta needed to be in agreement within 25%. We required that the distance between the track start points and the vertex is smaller than the corresponding distance between the track end points and the vertex. We also demanded that the distance between the start points of the two candidate tracks is smaller than the distance between the two end points. More details are provided in the Supplemental Material.

Further reduction of the cosmic tracks and minimization of bin-migration effects is achieved by considering only fully contained candidate muon-proton pairs within a fiducial volume of 10 cm inside the edge of the detector active volume. We retain 9051 data events that satisfy all event selection criteria.

In order to provide an accurate description of the dominant cosmic backgrounds pertinent to surface detectors, the full Monte Carlo (MC) simulation consists of a combination of simulated neutrino interactions overlaid on top of beam-off background data. This approach has been extensively used by MicroBooNE [19, 31–33]. The `GENIE v3.0.6` event generator is used to simulate neutrino interactions with the `G18_10a_02_11a` configuration [34, 35]. The CCQE and CCMEC predictions have been additionally tuned to T2K ν_μ-carbon CC0π data [36, 37]. We refer to the corresponding prediction as `G18`. All the final state particles following the primary neutrino interaction are generated by `GENIE`. They are further propagated in `GENIE` through the nucleus to account for FSI. The propagation of the particles outside the nucleus is simulated using `GEANT4` [38]. The MicroBooNE detector response is modeled using the `LArSoft` framework [39, 40]. Based on this MC prediction, we obtain a purity of $\approx 70\%$ and an efficiency for selecting CC1p0π events of $\approx 10\%$.

IV. OBSERVABLES

In neutrino-nucleus scattering events, there is an imbalance between the true initial neutrino momentum and the true sum of final-state lepton and hadron momenta as a result of nuclear effects [14]. A schematic representation of the kinematic imbalance variables of interest in this work is shown in Fig. 1.

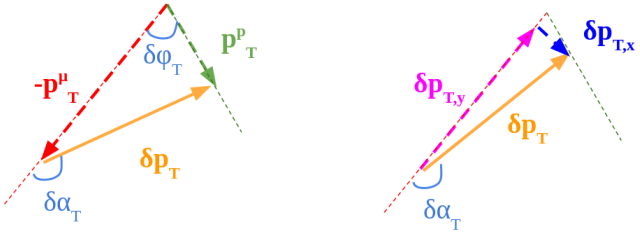

FIG. 1. Schematic representation of the kinematic imbalance variables on the plane transverse to the beam direction using CC1p0π events.

Using the CC1p0π candidate muon-proton pair kinematics, the missing momentum in the plane transverse to the beam direction is defined as

$$\delta p_T = |\vec{p}_T{}^{\,\mu} + \vec{p}_T{}^{\,p}|, \tag{1}$$

where $\vec{p}_T{}^{\,\mu}$ and $\vec{p}_T{}^{\,p}$ are the projections of the momenta of the outgoing lepton and proton on the transverse plane, respectively. In the absence of nuclear effects, purely QE interactions would yield $\delta p_T = 0$. In the presence of the

dense nuclear medium, this variable encapsulates information related to the Fermi motion, but it is smeared due to FSI and non-QE interactions, as can be seen in Fig. 2. Further discussion on the FSI smearing effects can be found in the Supplemental Material.

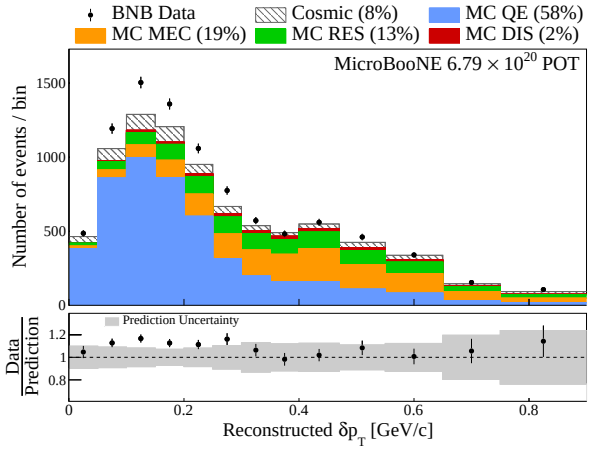

FIG. 2. Distribution of the selected CC1p0π events as a function of the transverse missing momentum δp_T. Only statistical uncertainties are shown on the data. The interaction contributions are obtained from simulation. The bottom panel shows the ratio of data to prediction.

The direction of the transverse momentum imbalance δp_T is described by the angle

$$\delta\alpha_T = \arccos\left(\frac{-\vec{p}_T{}^{\,\mu}\cdot\delta\vec{p}_T}{p_T{}^{\,\mu}\;\delta p_T}\right), \tag{2}$$

which is uniformly distributed in the absence of FSI due to the isotropic nature of the Fermi motion. In the presence of FSI, the proton momentum is generally reduced and the $\delta\alpha_T$ distribution becomes weighted towards 180°, as can be seen in Fig. 3.

The opening angle $\delta\phi_T$ between the correlated candidate muon-proton pair on the transverse plane is given by

$$\delta\phi_T = \arccos\left(\frac{-\vec{p}_T{}^{\,\mu}\cdot\vec{p}_T{}^{\,p}}{p_T{}^{\,\mu}\;p_T{}^{\,p}}\right). \tag{3}$$

In the absence of nuclear effects, QE events would be concentrated at $\delta\phi_T = 0$. When nuclear effects are present, QE events can occupy wider angles. At the same time, non-QE events are dominant in the high $\delta\phi_T$ part of the tail and their contribution is fairly flat across all angles, as can be seen in Fig. 4.

The muon-proton momentum imbalances transverse and longitudinal to the transverse lepton momentum [17] are defined as

$$\begin{aligned}\delta p_{T,x} &= (\hat{p}_\nu \times \hat{p}_T^{\,\mu})\cdot\delta\vec{p}_T\\ \delta p_{T,y} &= -\hat{p}_T^{\,\mu}\cdot\delta\vec{p}_T,\end{aligned} \tag{4}$$

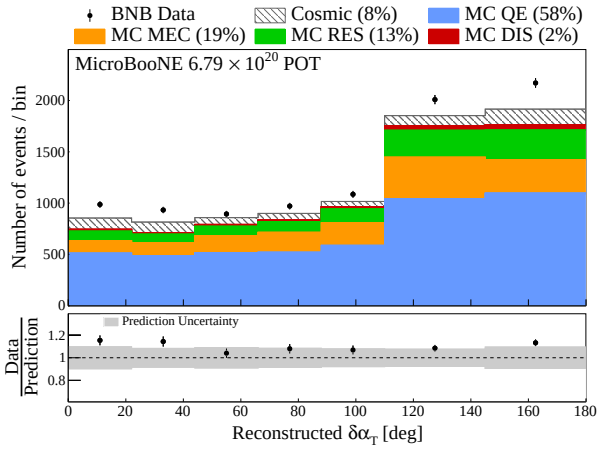

FIG. 3. Distribution of the selected CC1p0π events as a function of the transverse missing momentum direction $\delta\alpha_T$. Only statistical uncertainties are shown on the data. The interaction contributions are obtained from simulation. The bottom panel shows the ratio of data to prediction.

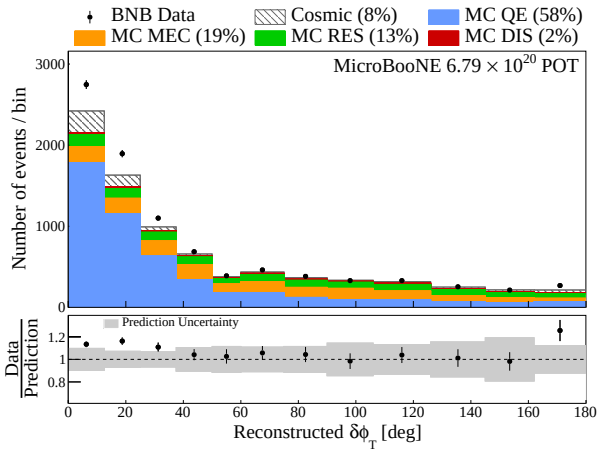

FIG. 4. Distribution of the selected CC1p0π events as a function of the muon-proton transverse opening angle $\delta\phi_T$. Only statistical uncertainties are shown on the data. The interaction contributions are obtained from simulation. The bottom panel shows the ratio of data to prediction.

and can also be written as

$$\begin{aligned}\delta p_{T,x} &= \delta p_T\cdot\sin\delta\alpha_T\\ \delta p_{T,y} &= \delta p_T\cdot\cos\delta\alpha_T.\end{aligned} \tag{5}$$

These distributions can be seen in Fig. 5 and Fig. 6, respectively. The $\delta p_{T,x}$ distribution is symmetric around $0\,\mathrm{GeV}/c$ due to the presence of the $\sin\delta\alpha_T$ factor in Eq. 5 and the fact that $\delta\alpha_T$ ranges from 0° to 180°. The width of the distribution is driven by the Fermi motion that affects the δp_T magnitude. Unlike $\delta p_{T,x}$, the $\delta p_{T,y}$ distribution is asymmetric with an enhanced contribution from negative values. The asymmetry is driven by the

presence of the $\cos\delta\alpha_T$ factor in Eq. 5 and the fact that $\delta\alpha_T$ is mainly peaked around 180°. Given that the forward $\delta\alpha_T$ peak is driven by FSI, the size of the $\delta p_{T,y}$ asymmetry is also sensitive to the FSI strength.

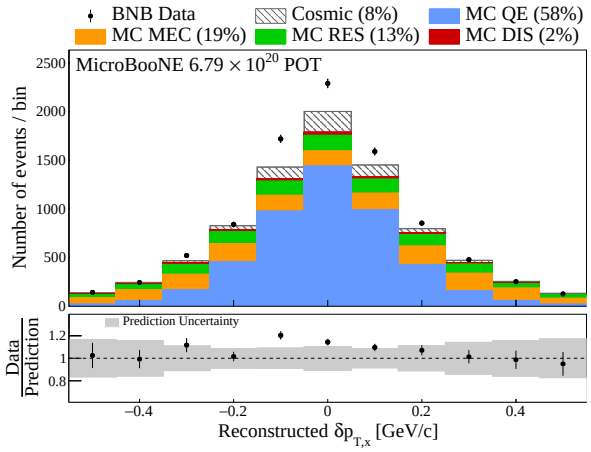

FIG. 5. Distribution of the selected CC1p0π events as a function of the perpendicular component of the transverse missing momentum $\delta p_{T,x}$. Only statistical uncertainties are shown on the data. The interaction contributions are obtained from simulation. The bottom panel shows the ratio of data to prediction.

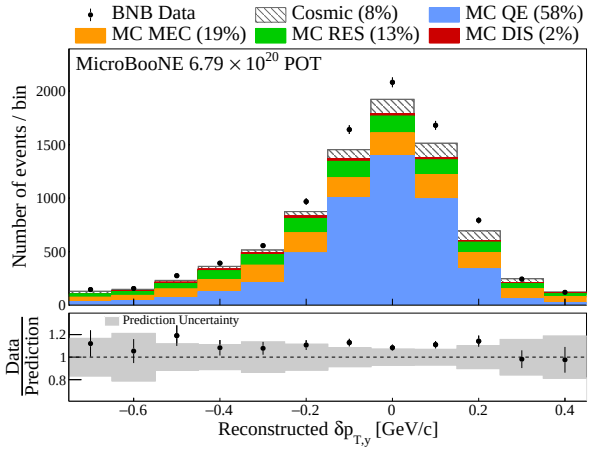

FIG. 6. Distribution of the selected CC1p0π events as a function of the longitudinal component of the transverse missing momentum $\delta p_{T,y}$. Only statistical uncertainties are shown on the data. The interaction contributions are obtained from simulation. The bottom panel shows the ratio of data to prediction.

Finally, the calorimetric energy reconstruction

$$E^{Cal} = E_\mu + T_p + BE \tag{6}$$

is investigated, where E_μ is the muon energy, T_p is the proton kinetic energy and $BE = 0.04\,\mathrm{GeV}/c$ is the average binding energy for argon [41]. This energy estimator, shown in Fig. 7, is an approximation for the true energy of the incoming neutrino and is used in oscillation searches.

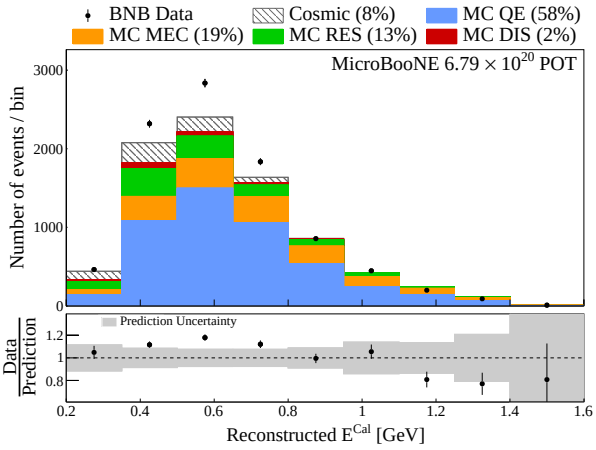

FIG. 7. Distribution of the selected CC1p0π events as a function of the calorimetric energy reconstruction E^{Cal}. Only statistical uncertainties are shown on the data. The interaction contributions are obtained from simulation. The bottom panel shows the ratio of data to prediction.

V. CROSS SECTION EXTRACTION & SYSTEMATICS

The flux-averaged differential event rate as a function of a given variable x in bin i is obtained by

$$\frac{dR}{dx_i} = \frac{N_i - B_i}{T \cdot \Phi_\nu \cdot \Delta_i} \tag{7}$$

where N_i and B_i are the number of measured events and the expected background events, respectively. T is the number of target argon nuclei in the fiducial volume of interest. Φ_ν corresponds to the integrated BNB flux and Δ_i corresponds to the i-th bin width or area for the single- and double-differential results, respectively.

We report the extracted cross sections for CC1p0π interactions using the Wiener singular value decomposition (Wiener-SVD) unfolding technique as a function of unfolded kinematic variables [42]. This unfolding procedure corrects a measured event rate for inefficiency and resolution effects. This is achieved by performing a minimization of a χ^2 score that compares data to a prediction and allows for a regularization term. A Wiener filter determines the level of regularization that is required to minimize the mean square error between the variance and bias of the result. In addition to the measured event rate, the method uses a covariance matrix calculated from simulated events accounting for the statistical and systematic uncertainties on the measurement as input. It also requires the construction of a response matrix describing

the expected detector smearing and reconstruction efficiency.

The output of the method is an unfolded differential cross section, a covariance matrix describing the total uncertainty on the unfolded result, and an additional smearing matrix that we refer to as A_C. The latter contains information about the regularization and bias of the measurement. The corresponding A_C matrices have been applied to all the cross section predictions included in this work when a comparison to the unfolded data is performed. The A_C matrix should be applied to any independent theoretical prediction when a comparison is performed to the data reported in this paper. The data release, the unfolded covariance matrices, and the additional matrices A_C can be found in the Supplemental Material.

The total covariance matrix $E_{ij} = E_{ij}^{\text{stat}} + E_{ij}^{\text{syst}}$ includes the statistical and systematic uncertainties on the differential event rate associated with our measurement. E_{ij}^{stat} is a diagonal covariance matrix with the statistical uncertainties and E_{ij}^{syst} is a covariance matrix that incorporates the total systematic uncertainties detailed below.

The neutrino flux is predicted using the flux simulation of the MiniBooNE collaboration that used the same beam line [43]. Neutrino cross section modeling uncertainties were estimated using the `GENIE` framework of event reweighting [34, 35, 37]. The rescattering uncertainties were obtained using `GEANT4` and the relevant reweighting package [44]. For each of these sources of uncertainty, we use a multisim technique [45], which consists of generating a large number of MC replicas, each one called a "universe", where model parameters are varied within their uncertainties. The simultaneous varying of many model parameters provides a correct treatment of their correlations. A total of n such universes are used to construct a covariance matrix corresponding to each source of uncertainty,

$$E_{ij} = \frac{1}{n}\sum_{k=1}^{k=n}\left(R_i^k - R_i^{CV}\right)\cdot\left(R_j^k - R_j^{CV}\right) \qquad (8)$$

where R_i^{CV} (R_j^{CV}) and R_i^k (R_j^k) are the flux-averaged event rates for the central value and systematic universe k in a measured bin i (j), respectively. The resulting covariance matrices are summed together to estimate the relevant uncertainty from each source.

An additional cross section uncertainty using the `NuWro v19.02.2` event generator prediction [46] as an alternative universe has been added. The relevant modeling is detailed in section VI. The flux-integrated `NuWro` cross sections are obtained using Eq. 7 and the corresponding covariance matrices are constructed using Eq. 8 and a single universe ($n = 1$).

For detector model systematic uncertainties, one detector parameter is varied each time by 1σ and is referred to as a "unisim". These include variations in the light yield, the ionization electron recombination model, space-charge effects, and waveform deconvolution [47]. We then examine the impact of each parameter variation on the MC event rates by obtaining the differences with respect to the central value on a bin-by-bin basis. We define the total detector 1σ systematic uncertainty by summing in quadrature the effect of m detector variations using the formalism introduced in Eq. 8,

$$E_{ij} = \sum_{k=1}^{k=m}\left(R_i^k - R_i^{CV}\right)\cdot\left(R_j^k - R_j^{CV}\right). \qquad (9)$$

The full fractional uncertainty on the integrated total cross section is 11% and includes contributions from the neutrino flux prediction (7.3%), neutrino interaction cross section modeling (5.3%), detector response modeling (4.9%), beam exposure (2.3%), statistics (1.5%), number-of-scattering-targets (1.2%), reinteractions (1%), and out-of-cryostat interaction modeling (0.2%).

In the results presented below, the inner error bars on the reported cross sections correspond to the statistical uncertainties. The systematic uncertainties were decomposed into shape- and normalization-related sources following the procedure outlined in [48]. The cross-term uncertainties were incorporated in the normalization part. The outer error bars on the reported cross sections correspond to statistical and shape uncertainties added in quadrature. The normalization uncertainties are presented with the gray band at the bottom of each plot. Overflow (underflow) values are included in the last (first) bin.

VI. MODELING CONFIGURATIONS

The nominal MC neutrino interaction prediction (`G18`) uses the local Fermi gas (LFG) model [49], the Nieves CCQE scattering prescription [50] which includes Coulomb corrections for the outgoing muon [51] and random phase approximation (RPA) corrections [52]. Additionally, it uses the Nieves MEC model [53], the KLN-BS RES [54–57] and Berger-Sehgal coherent (COH) [58] scattering models, the hA2018 FSI model [59], and MicroBooNE-specific tuning of model parameters [37].

Our results are also compared to a number of alternative event generators. `GiBUU 2021 (GiBUU)` uses similar models, but they are implemented in a coherent way by solving the Boltzmann-Uehling-Uhlenbeck transport equation [60]. The modeling includes the LFG model [49], a standard CCQE expression [61], an empirical MEC model and a dedicated spin dependent resonance amplitude calculation following the `MAID` analysis [60]. The DIS model is from `PYTHIA` [62]. `GiBUU`'s FSI treatment propagates the hadrons through the residual nucleus in a nuclear potential which is consistent with the initial state. `NuWro v19.02.2 (NuWro)` uses the LFG model [49], the Llewellyn Smith model for QE events [63], the Nieves model for MEC events [64], the Adler-Rarita-Schwinger formalism to calculate the

Δ resonance explicitly [57], the BS COH [58] scattering model and an intranuclear cascade model for FSI [64]. `NEUT v5.4.0 (NEUT)` uses the LFG model [49], the Nieves CCQE scattering prescription [50], the Nieves MEC model [53], the BS RES [54–57] and BS COH [58] scattering models, and FSI with Oset medium corrections for pions [34, 35].

In addition to the alternative event generators, our results are compared to a number of different `GENIE` configurations. These include an older version, `GENIE v2.12.10 (Gv2)` [34, 35], which uses the Bodek-Ritchie Fermi Gas model, the Llewellyn Smith CCQE scattering prescription [63], the empirical MEC model [65], a Rein-Sehgal RES and COH scattering model [66], and a data driven FSI model denoted as "hA" [67]. Another model, "`Untuned`", uses the `GENIE v3.0.6 G18_10a_02_11a` configuration without additional MicroBooNE-specific tuning. Finally, the newly added theory-driven `GENIE v3.2.0 G21_11b_00_000` configuration (`G21`) is shown. This includes the SuSAv2 prediction for the QE and MEC scattering parts [68] and the hN2018 FSI model [69]. The modeling options for RES, DIS, and COH interactions are the same as for `G18`.

The χ^2/bins data comparison for each generator shown on all the figures takes into account the total covariance matrix. Theoretical uncertainties on the models themselves are not included.

VII. RESULTS

Along with the aforementioned kinematic imbalance and energy estimator results, the data are also presented as a function of the lepton angular orientation (Fig. 8). Previous MicroBooNE measurements using different signal definitions [19, 70, 71] showed discrepancies in that quantity, primarily in the forward direction. These analyses used an older simulation prediction, namely `GENIE v2.12.2`, to account for the efficiency corrections and beam-induced backgrounds. This work illustrates that all generator (Fig. 8a) and `GENIE` configuration (Fig. 8b) predictions are in good agreement with the data when reported as a function of $\cos\theta_\mu$.

Figures 9 and 10 show the measured single-differential cross sections as a function of δp_T using all the events (panel a), as well as the double-differential results as a function of the same kinematic variable in $\delta\alpha_T$ bins (panels b-e). In the presence of FSI, the proton can rescatter or be absorbed, yielding larger kinematic imbalances on the transverse plane and δp_T values that extend beyond the Fermi momentum. Furthermore, the same extended tail can be obtained when pions produced due to multi-nucleon effects (MEC or RES) are either absorbed or below the detection threshold. The single-differential result shows such a high-momentum tail that extends above 0.8 GeV/c. This picture is consistent with the results reported by the T2K and MINERvA collaborations [15, 16, 72]. Unlike the single-differential result, the double differential results with low $\delta\alpha_T$ extend only slightly above 0.4 GeV/c. That indicates that this region contains minimal FSI and multi-nucleon effects and the δp_T distribution is driven by the nucleon Fermi motion. On the other hand, the higher $\delta\alpha_T$ values correspond to δp_T distributions that extend beyond 0.8 GeV/c. This behavior is indicative of the presence of FSI and multi-nucleon effects that smear the δp_T distribution to higher values. Future multi-differential results can help further disentangle the contributions from these effects. Figure 9 shows the comparisons to a number of available neutrino event generators with `NuWro` and `G18` showing the best agreement over all events. Figure 10 shows the same results compared to a number of `GENIE` configurations illustrating that `Gv2` is disfavored, an observation that is driven by the `Gv2` low δp_T behavior. Furthermore, `Untuned` shows a good χ^2/bins performance across all slices but predicts lower values than data.

Figure 11 shows the double-differential results as a function of δp_T in $\cos\theta_\mu$ bins. In a factorized nuclear model such as the LFG, the Fermi motion part of δp_T should stay constant in terms of the shape as a function of the outgoing lepton kinematics, since in such models the initial state nucleon momentum is a property of the nucleus that cannot be affected by the interaction momentum or energy transfer. That is indeed the observed behavior in the reported results across all event generators and configurations, where no evidence of the inadequacy of the factorization approach is observed. Figure 11 shows the comparisons to a number of available neutrino event generators, where the `G18` prediction is favored based on the χ^2/ndf results. Apart from the factorization, a better separation between QE and non-QE can be gained depending on the $\cos\theta_\mu$ region. As can be seen in Fig. 12 for `G18`, MEC events play a more pronounced role for forward muon scattering and in the high δp_T tail, as opposed to backward scattering angles, which are much more strongly populated by QE events. Furthermore, the `G18` cross section prediction falls below the data in the $-1 < \cos\theta_\mu < 0.5$ region, as seen in Fig. 12a and Fig. 12b. That could indicate that additional contribution from the QE part of the `G18` prediction is needed beyond the MicroBooNE tune. Figure 13 shows the same interaction breakdown for `GiBUU`. Unlike `G18`, `GiBUU` illustrates a peak shift to the right, which becomes more pronounced in the backward direction. This shift is driven by the enhanced MEC contribution in higher δp_T values and the reduced QE contribution at smaller values. In the backward direction, `GiBUU` further shows a cross section excess driven by the MEC contribution. Figure 14 shows the same results compared to a number of `GENIE` configurations illustrating that `Gv2` is disfavored due to the low δp_T bin behavior.

Figures 15 and 16 show the double-differential cross section as a function of δp_T in $\cos\theta_p$ bins. The factorization of the nuclear motion is mostly preserved in $\cos\theta_p$ bins, analogously to the previous result in $\cos\theta_\mu$. Fig-

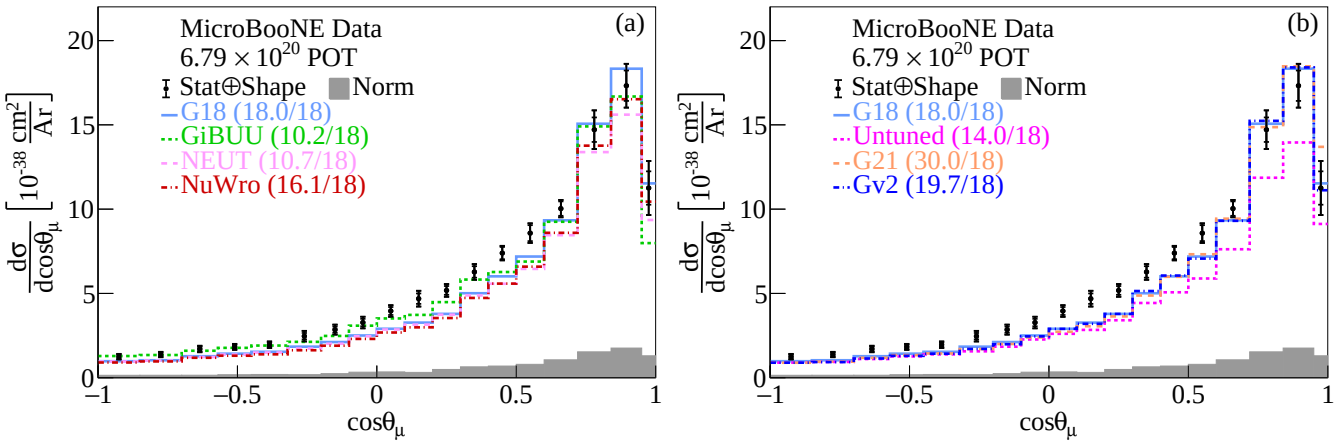

FIG. 8. The flux-integrated single-differential cross sections as a function of $\cos\theta_\mu$. (a) Generator and (b) GENIE configuration predictions are compared to data. Inner and outer error bars show the statistical and total (statistical and shape systematic) uncertainty at the 1σ, or 68%, confidence level. The gray band shows the normalization systematic uncertainty. The numbers in parentheses show the χ^2/bins calculation for each one of the predictions.

ure 15 shows the comparisons to a number of available neutrino event generators. The GiBUU prediction is significantly lower than the data in the backward proton angle for low δp_T values, as shown in Fig. 15a. Figure 16 shows the same results compared to a number of GENIE configurations illustrating that Gv2 is disfavored across all $\cos\theta_p$ bins. As can be seen in Fig. 17, this particularly poor performance is driven by the QE contribution. For backward scattering events (panel a), the QE contribution predicted by Llewellyn Smith is significantly overestimated. For intermediate angles ($0 < \cos\theta_p < 0.5$), the same QE model results in an unphysical double peak. For forward scattering ($0.5 < \cos\theta_p < 1$), the Gv2 QE prediction yields a pronounced contribution at lower values of δp_T compared to the data.

Figures 18 and 19 show the single-differential cross sections as a function of $\delta\alpha_T$ using all the events (panel a), as well as the double-differential results in the same kinematic variable in δp_T bins (panels b-d). The single-differential results shown in panel a yield some interesting observations when compared to the relevant T2K and MINERvA results [15, 16, 72]. Our distribution illustrates a slightly asymmetric behavior, similar to the one reported by the T2K collaboration at a comparable energy with MicroBooNE. Within the precision of the data sets, the mass-number dependence of the nuclear effects seems to be reasonably well-modeled. Unlike our result, the measurement by MINERvA reports a more pronounced asymmetry on hydrocarbon. The breakdown plots in Fig. 18 in Ref. [72] show that this behavior is driven by enhanced pion-production rates due to the higher average beam energy. Low δp_T values result in a fairly uniform $\delta\alpha_T$ distribution indicative of the absence of FSI effects in that part of the phase-space. On the other hand, higher δp_T values result in a highly asymmetric $\delta\alpha_T$ distribution, which is driven by the strength of the FSI interactions. Figure 18 shows the comparisons to a number of available neutrino event generators, where NuWro is the generator with the most conservative FSI strength. Figure 19 shows the same results compared to a number of GENIE configurations, where Gv2 yields the highest χ^2/bins result, especially in the lowest δp_T region. As shown in Fig. 20, this is driven by the Gv2 QE performance, which results in peaks at the edges of the distribution, unlike the data result.

Figures 21 and 22 show the double-differential results as a function of $\delta\alpha_T$ in $\cos\theta_\mu$ bins. All the bins illustrate an asymmetric $\delta\alpha_T$ distribution, with the exception of the region where $\cos\theta_\mu \approx 1$, with the latter implying that this part of phase-space includes events with minimal FSI effects. Figure 21 shows the comparisons to a number of available neutrino event generators with GiBUU giving the best performance. Figure 22 shows the same results compared to a number of GENIE configurations, illustrating that Gv2 is disfavored in the region where $\cos\theta_\mu < 0.75$.

Figures 23 and 24 show the double-differential cross sections as a function of $\delta\alpha_T$ in $\cos\theta_p$ bins. The results in the region with $0 < \cos\theta_p < 0.75$ show a fairly flat distribution. The cross section distributions corresponding to forward and backward proton scattering exhibit an FSI-driven asymmetric behavior. Figure 23 shows the comparisons to a number of available neutrino event generators, where NuWro yields a prediction that is disfavored for forward scattering. Figure 24 shows the same results compared to a number of GENIE configurations, illustrating that Gv2 is disfavored across all $\cos\theta_p$ bins. In the -1 $< \cos\theta_p < 0$ region shown in Fig. 24a, all the predictions illustrate a peak close to 180° with the exception of Gv2. The driving force for this difference is the Gv2 QE contribution, as can be seen in Fig. 25. This is indicative of potential modeling issues in the Llewellyn Smith QE cross section and of the hA FSI performance used in the

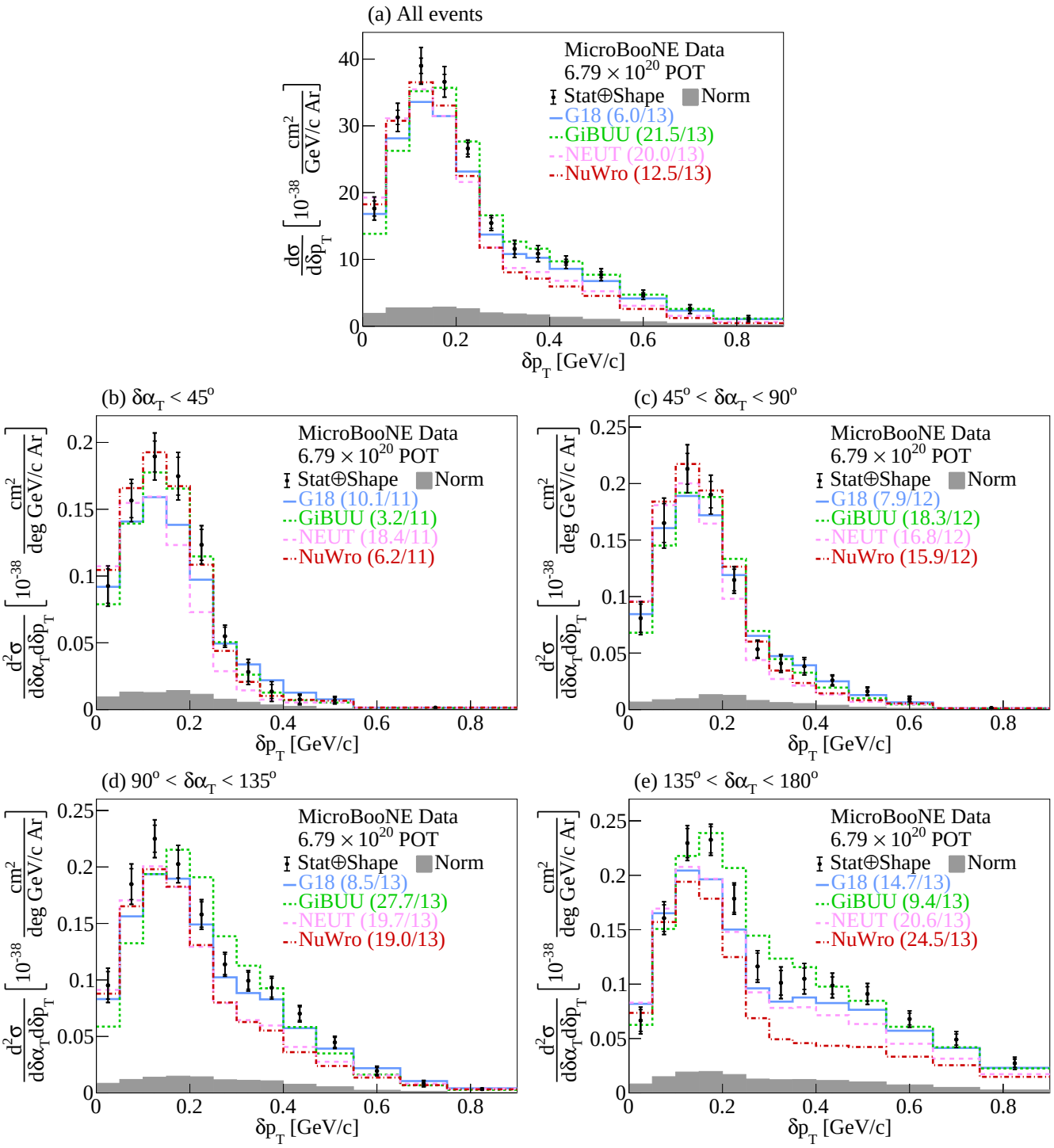

FIG. 9. The flux-integrated (a) single- and (b-e) double- (in $\delta\alpha_T$ bins) differential cross sections as a function of δp_T. Inner and outer error bars show the statistical and total (statistical and shape systematic) uncertainty at the 1σ, or 68%, confidence level. The gray band shows the normalization systematic uncertainty. Colored lines show the results of theoretical cross section calculations using the `G18 GENIE` (blue), `GiBUU` (green), `NEUT` (pink), and `NuWro` (red) event generators. The numbers in parentheses show the χ^2/bins calculation for each one of the predictions.

`Gv2` prediction. Unlike `Gv2`, the theory-driven `GENIE v3` family of predictions (`G18`, `Untuned`, and `G21`) closely follow the data.

Figures 26 and 27 show the single-differential cross sections as a function of $\delta\phi_T$ using all the events (panel a), as well as the double-differential results as a func-

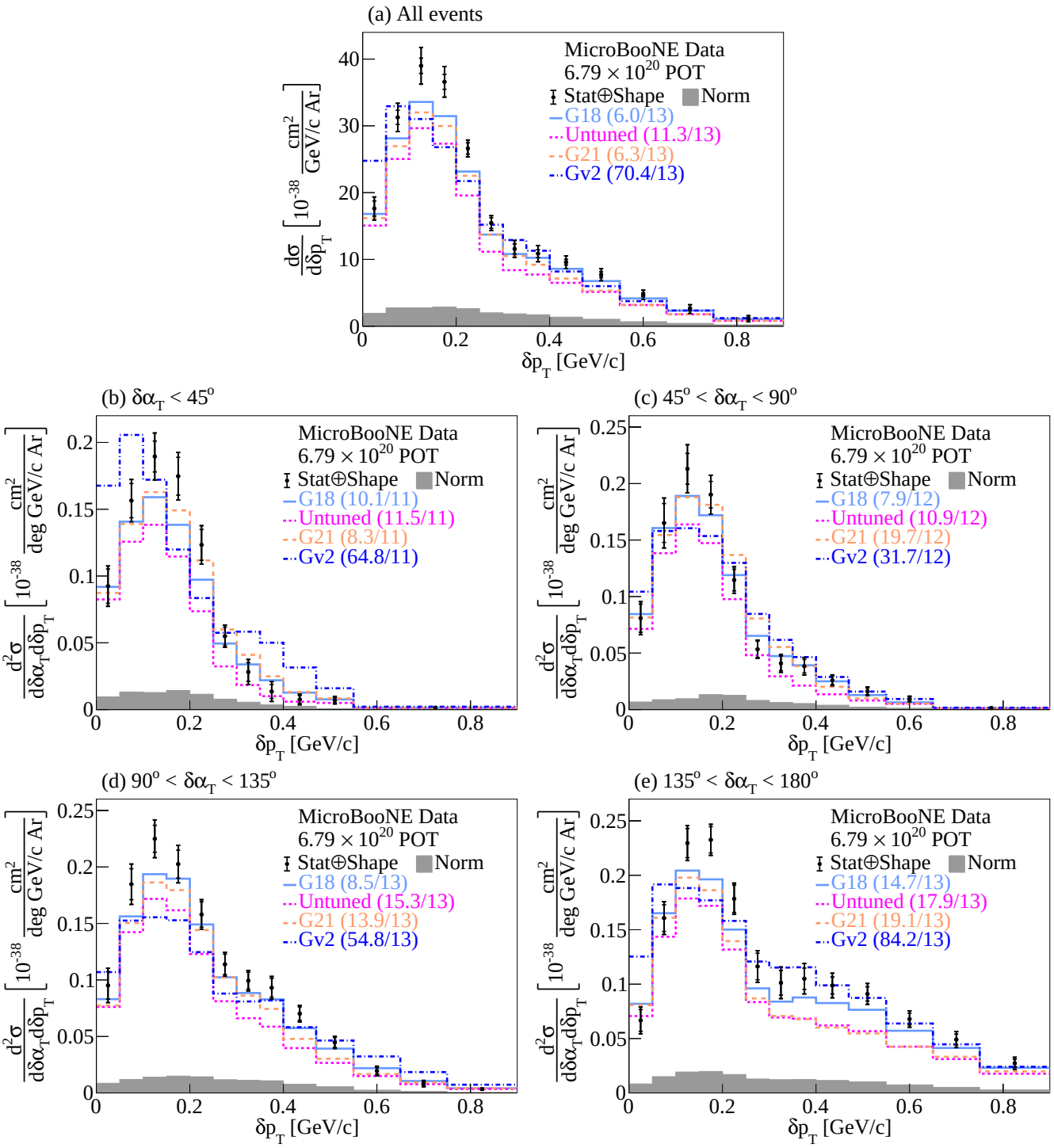

FIG. 10. The flux-integrated (a) single- and (b-e) double- (in $\delta\alpha_T$ bins) differential cross sections as a function of δp_T. Inner and outer error bars show the statistical and total (statistical and shape systematic) uncertainty at the 1σ, or 68%, confidence level. The gray band shows the normalization systematic uncertainty. Colored lines show the results of theoretical cross section calculations using the `G18` (light blue), `Untuned` (magenta), `G21` (orange), and `Gv2` (dark blue) `GENIE` configurations. The numbers in parentheses show the χ^2/bins calculation for each one of the predictions.

tion of the same kinematic variable in δp_T bins (panels b-d). Figure 26 shows the comparisons to a number of available neutrino event generators, with all the generators illustrating a fairly good performance. This result is consistent with the one reported by the T2K collaboration [15, 72]. In the lowest δp_T region shown in panel b,

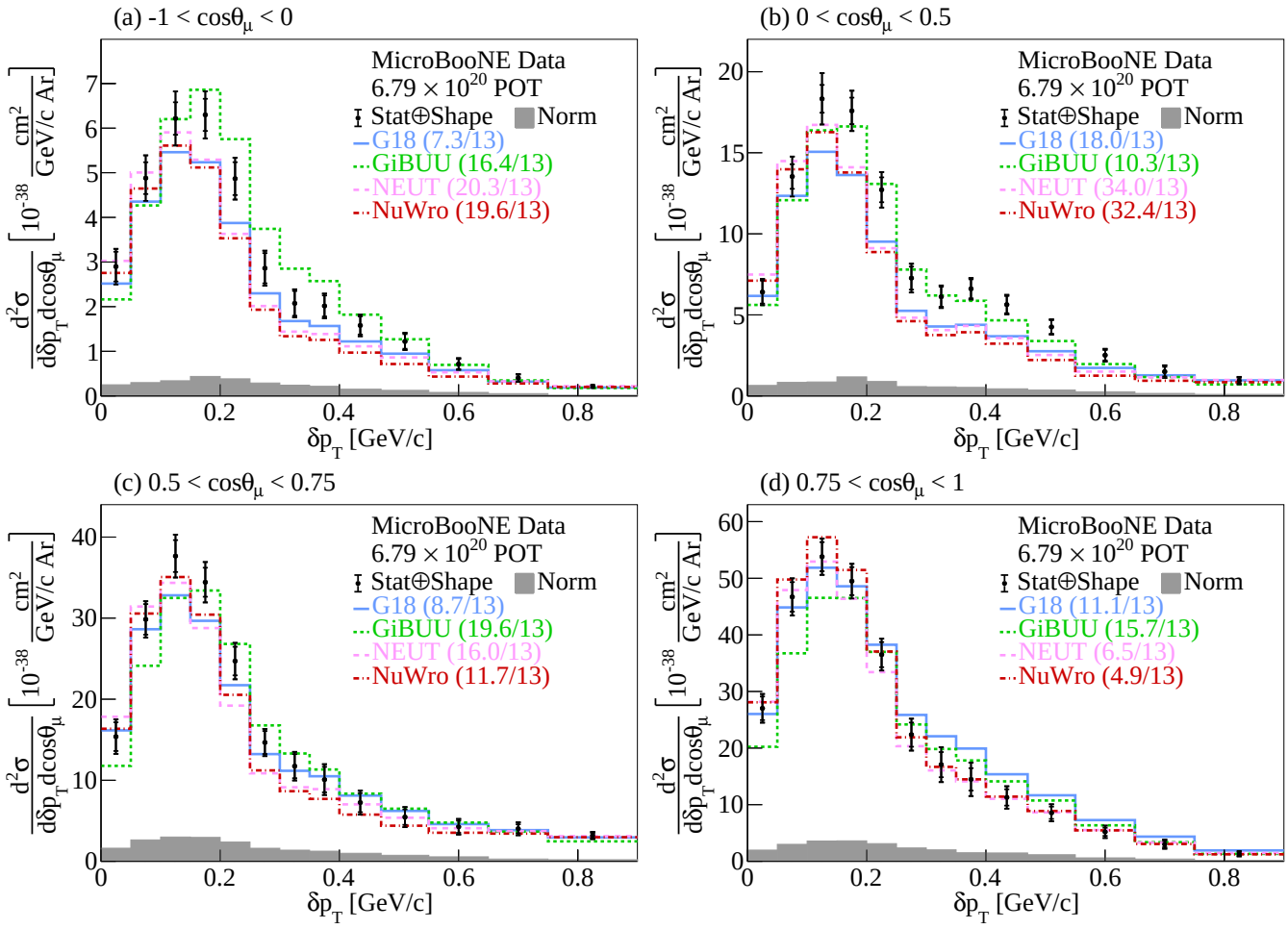

FIG. 11. The flux-integrated double-differential cross sections as a function of δp_T in $\cos\theta_\mu$ bins. Inner and outer error bars show the statistical and total (statistical and shape systematic) uncertainty at the 1σ, or 68%, confidence level. The gray band shows the normalization systematic uncertainty. Colored lines show the results of theoretical cross section calculations using the `G18 GENIE` (blue), `GiBUU` (green), `NEUT` (pink), and `NuWro` (red) event generators. The numbers in parentheses show the χ^2/bins calculation for each one of the predictions.

`NuWro` is the generator with the best performance. Figure 27 shows the same results compared to a number of `GENIE` configurations, where `Gv2` is disfavored in all regions. At small δp_T values the cross section is decreasing and zero above $\approx 40°$ which indicates the absence of multi-nucleon and FSI effects. Higher δp_T values lead to $\delta\phi_T$ cross sections that extend up to 180°. This behavior is primarily driven by multi-body effects with hadrons below the detection threshold that introduce large kinematic imbalances, as can be seen in panels c-d of Fig. 28.

Figures 29 and 30 show the single-differential cross sections as a function of $\delta p_{T,x}$ using all the events (panel a), as well as the double-differential results in the same kinematic variable in $\delta p_{T,y}$ slices (panels b-c). Figure 29 shows the comparisons to a number of available neutrino event generators. The central region with $|\delta p_{T,y}| < 0.15\,\text{GeV}/c$ is dominated by QE interactions, while the broader distributions with $|\delta p_{T,y}| > 0.15\,\text{GeV}/c$ are mainly driven by MEC events, as can be seen in Fig. 31. In the MEC dominated region of $\delta p_{T,y} <$ -0.15 GeV/c, all the generators, apart from `GiBUU`, seem to be lacking in terms of the peak strength. `GiBUU` seems to be overestimating that MEC contribution in the $\delta p_{T,y} <$ -0.15 GeV/c bin. With the exception of `NEUT`, all the event generators illustrate a good performance in the $|\delta p_{T,y}| < 0.15\,\text{GeV}/c$ region. Figure 30 shows the same results compared to a number of `GENIE` configurations, where `Gv2` shows the worst performance.

The aforementioned results in kinematic imbalance variables illustrate significant differences across the event generators and configurations used for comparison, especially in the case of the double-differential studies. Yet, the quantity that enters the oscillation probability is the true neutrino energy. Neutrino energy estimators, such as the calorimetric energy E^{Cal} defined in Eq. 6, are used as a proxy for the true quantity. The studies reported next present the results as a function of E^{Cal} in bins of the kinematic imbalance variables.

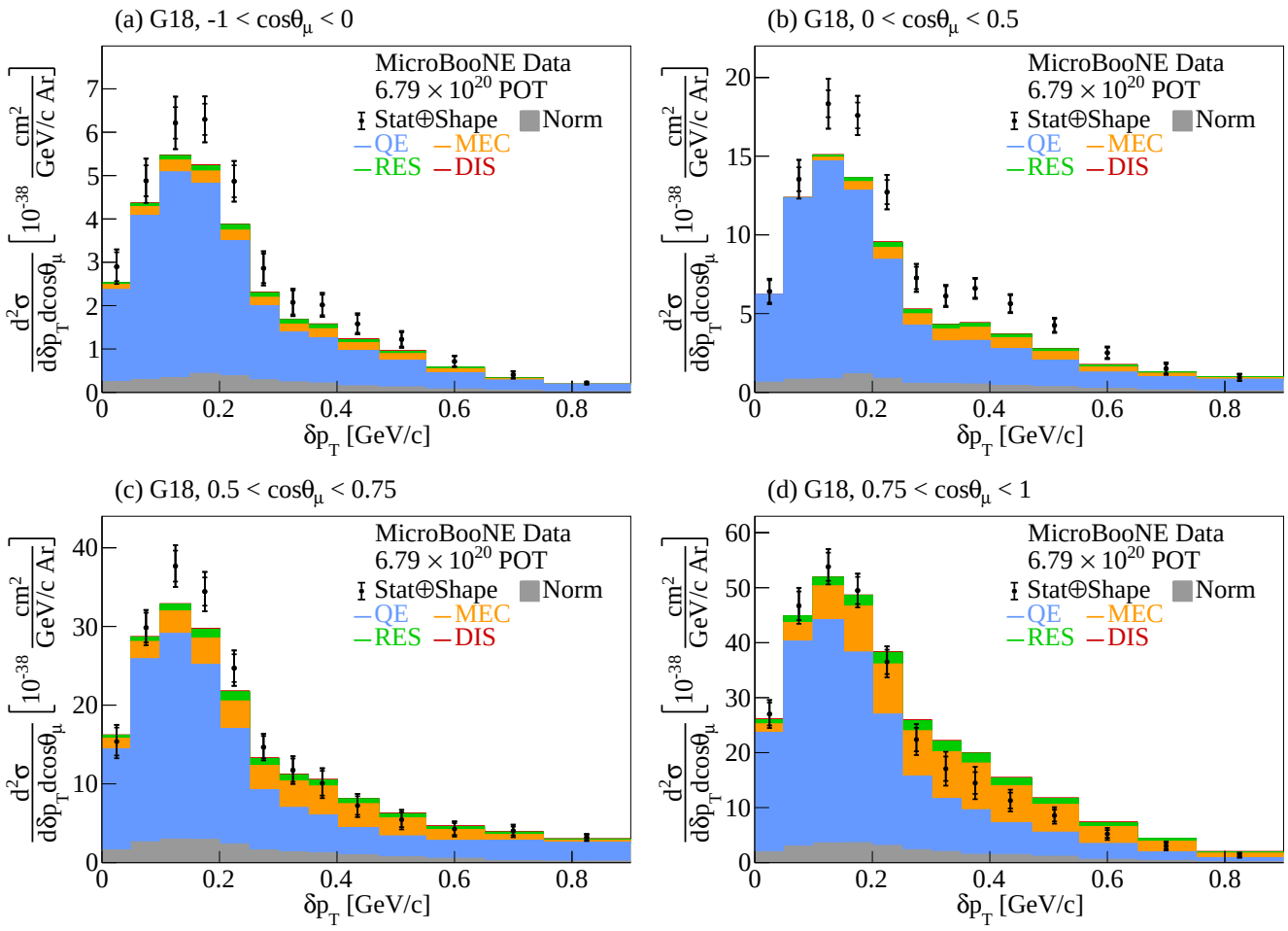

FIG. 12. Comparison between the flux-integrated double-differential cross sections as a function of δp_T for data and the `G18 GENIE` prediction in $\cos\theta_\mu$ bins. Inner and outer error bars show the statistical and total (statistical and shape systematic) uncertainty at the 1σ, or 68%, confidence level. The gray band shows the normalization systematic uncertainty. Colored stacked histograms show the results of theoretical cross section calculations using the `G18 GENIE` prediction for QE (blue), MEC (orange), RES (green), and DIS (red) interactions.

Figures 32 and 33 show the single-differential cross sections as a function of E^{Cal} using all the events (panel a), as well as the double-differential results in the same kinematic variable in δp_T bins (panels b-d). Figure 32 shows the comparisons to a number of available neutrino event generators, where the E^{Cal} distribution covers the same energy spectrum across all bins. All the event generators illustrate an equally good performance in the lowest δp_T bin. `NEUT` and `NuWro` show a deficit relative to the data in the highest δp_T bins. Figure 33 shows the same results compared to a number of `GENIE` configurations, where `G18` illustrates the best performance. Interestingly, all the alternative `GENIE` configurations illustrate a plateau in the highest δp_T bin.

Figures 34 and 35 show the double-differential results as a function of E^{Cal} in $\delta\alpha_T$ bins. Figure 34 shows the comparisons to a number of available neutrino event generators. Once again, the E^{Cal} distribution covers the same energy spectrum across all of our results and all the event generators show fairly good behavior. Figure 35 shows the same results compared to a number of `GENIE` configurations, where all the `GENIE` configurations except for `G18` illustrate shape and strength differences.

Figures 36 and 37 show the double-differential results as a function of E^{Cal} in $\delta p_{T,y}$ bins. Figure 36 shows the comparisons to a number of available neutrino event generators. All event generators predict very similar cross sections for $-0.15 < \delta p_{T,y} < 0.15\,\mathrm{GeV}/c$ (panel a). Unlike this central region, the $|\delta p_{T,y}| > 0.15\,\mathrm{GeV}/c$ results yield a wide spread across the generator predictions (panels b-c). Furthermore, apart from `GiBUU`, all the predictions lack strength in the $\delta p_{T,y} < -0.15\,\mathrm{GeV}/c$ bin (panel b). Additionally, `NEUT` illustrates the same deficit in the $\delta p_{T,y} > 0.15\,\mathrm{GeV}/c$ bin (panel c). Figure 37 shows the same results compared to a number of `GENIE` configurations, where all the `GENIE` configurations but `G18` illustrate a poor performance due to shape and strength issues.

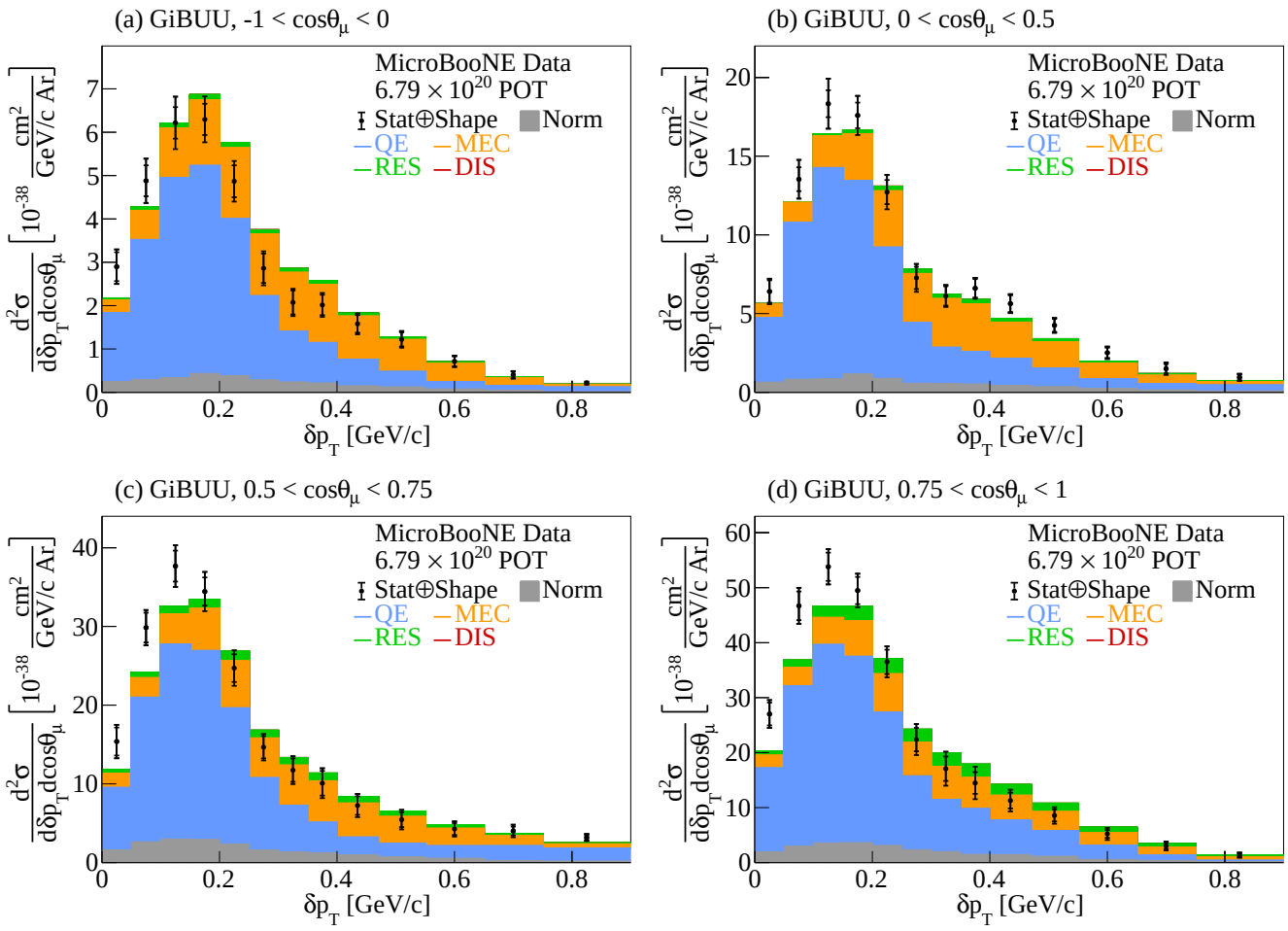

FIG. 13. Comparison between the flux-integrated double-differential cross sections as a function of δp_T for data and the GiBUU prediction in $\cos\theta_\mu$ bins. Inner and outer error bars show the statistical and total (statistical and shape systematic) uncertainty at the 1σ, or 68%, confidence level. The gray band shows the normalization systematic uncertainty. Colored stacked histograms show the results of theoretical cross section calculations using the `GiBUU` prediction for QE (blue), MEC (orange), RES (green), and DIS (red) interactions.

VIII. CONCLUSIONS

This work reports on measurements of flux-integrated differential cross sections for event topologies with a single muon and a single proton detected in the final state using the Booster Neutrino Beam at Fermi National Accelerator Laboratory and the MicroBooNE detector. The data were studied for the first time in the form of single-differential cross sections in kinematic imbalance variables on argon. Furthermore, the first double-differential cross sections in these variables were reported on the same nucleus. Additionally, novel double-differential cross section measurements of a neutrino energy estimator in bins of these variables were presented. The results were compared to a number of event generators and model configurations. The predictions as a function of the energy estimator across all generators and model configurations remain mostly unchanged regardless of the kinematic variable used for the double-differential measurements. The good agreement observed across the calorimetric energy distributions suggests that the energy dependence is largely well-modeled across all predictions. Unlike the energy estimator results, we found that the measured kinematic imbalance cross sections in different phase-space regions are sensitive to nuclear effects. The performance of the event generators and configurations varies depending on the observable of interest. Overall, the `GENIE v3.0.6 G18_10a_02_11a` cross section predictions with the MicroBooNE-specific tuning (`G18`) fit the data well. On the other hand, the `GENIE v2.12.10` (`Gv2`) cross section predictions are systematically a poor fit to data with significant shape differences across all variables of interest. The `GENIE v3.0.6 G18_10a_02_11a` configuration without additional tuning (`Untuned`) shows a systematic deficit of $\sim 20\%$ which necessitated the development of the aforementioned tune. The `GENIE v3.2.0 G21_11b_00_000` configuration (`G21`) serves as an example of a theory-

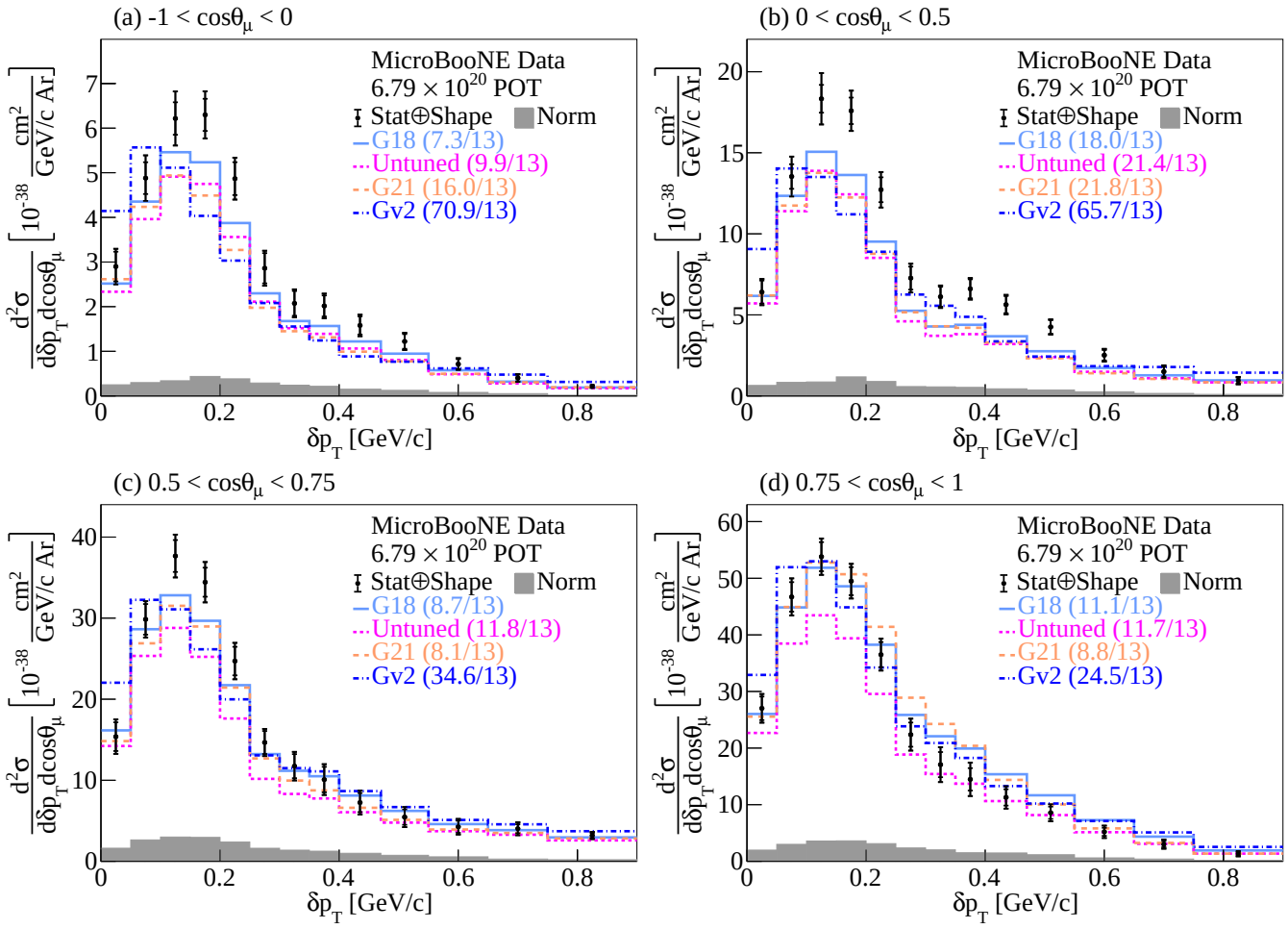

FIG. 14. The flux-integrated double-differential cross sections as a function of δp_T in $\cos\theta_\mu$ bins. Inner and outer error bars show the statistical and total (statistical and shape systematic) uncertainty at the 1σ, or 68%, confidence level. The gray band shows the normalization systematic uncertainty. Colored lines show the results of theoretical cross section calculations using the `G18` (light blue), `Untuned` (magenta), `G21` (orange), and `Gv2` (dark blue) `GENIE` configurations. The numbers in parentheses show the χ^2/bins calculation for each one of the predictions.

driven GENIE configuration that shows good agreement with data in most variables without the need for additional tuning. `GiBUU 2021` (`GiBUU`) shows good agreement with data in most kinematic variables, with the exception of δp_T, where a systematic shift to higher values of δp_T has been identified. A potential source of this shift is due to the `GiBUU` MEC modeling. The `NuWro v19.02.2` (`NuWro`) prediction falls bellow the data due to poor FSI modeling and shows significant shape differences in FSI-dominated parts of the phase-space. `NEUT v5.4.0` (`NEUT`) also results in predictions mostly falling below the data points. This mismodeling remains largely unnoticed when combined into the calorimetric energy estimator. Yet, future neutrino oscillation measurements will rely on accurate cross section predictions and a precise mapping between measured and true neutrino energies. Therefore, such mismodeling effects might impact their experimental sensitivity. The reported results both provide precision data to benchmark neutrino-nucleus interaction models and establish phase-space regions where precise reaction modeling is still needed.

IX. ACKNOWLEDGMENTS

This document was prepared by the MicroBooNE collaboration using the resources of the Fermi National Accelerator Laboratory (Fermilab), a U.S. Department of Energy, Office of Science, HEP User Facility. Fermilab is managed by Fermi Research Alliance, LLC (FRA), acting under Contract No. DE-AC02-07CH11359. MicroBooNE is supported by the following: the U.S. Department of Energy, Office of Science, Offices of High Energy Physics and Nuclear Physics; the U.S. National Science Foundation; the Swiss National Science Foundation; the Science and Technology Facilities Council (STFC), part of the United Kingdom Research and Innovation; the Royal Society (United Kingdom); the UK Research

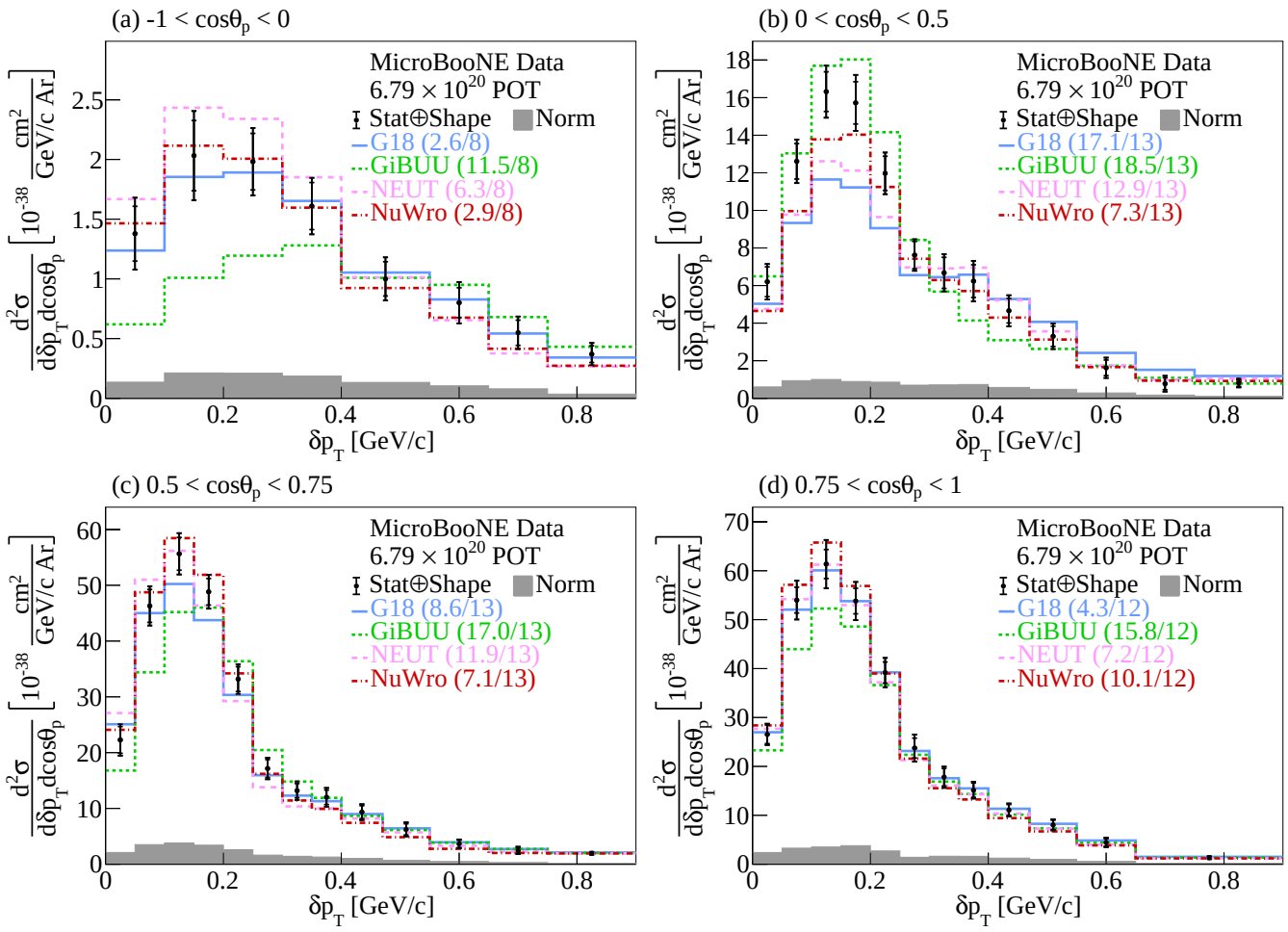

FIG. 15. The flux-integrated double-differential cross sections as a function of δp_T in $\cos\theta_p$ bins. Inner and outer error bars show the statistical and total (statistical and shape systematic) uncertainty at the 1σ, or 68%, confidence level. The gray band shows the normalization systematic uncertainty. Colored lines show the results of theoretical cross section calculations using the `G18 GENIE` (blue), `GiBUU` (green), `NEUT` (pink), and `NuWro` (red) event generators. The numbers in parentheses show the χ^2/bins calculation for each one of the predictions.

and Innovation (UKRI) Future Leaders Fellowship; and The European Union's Horizon 2020 Marie Sklodowska-Curie Actions. Additional support for the laser calibration system and cosmic ray tagger was provided by the Albert Einstein Center for Fundamental Physics, Bern, Switzerland. We also acknowledge the contributions of technical and scientific staff to the design, construction, and operation of the MicroBooNE detector as well as the contributions of past collaborators to the development of MicroBooNE analyses, without whom this work would not have been possible. For the purpose of open access, the authors have applied a Creative Commons Attribution (CC BY) license to any Author Accepted Manuscript version arising from this submission.

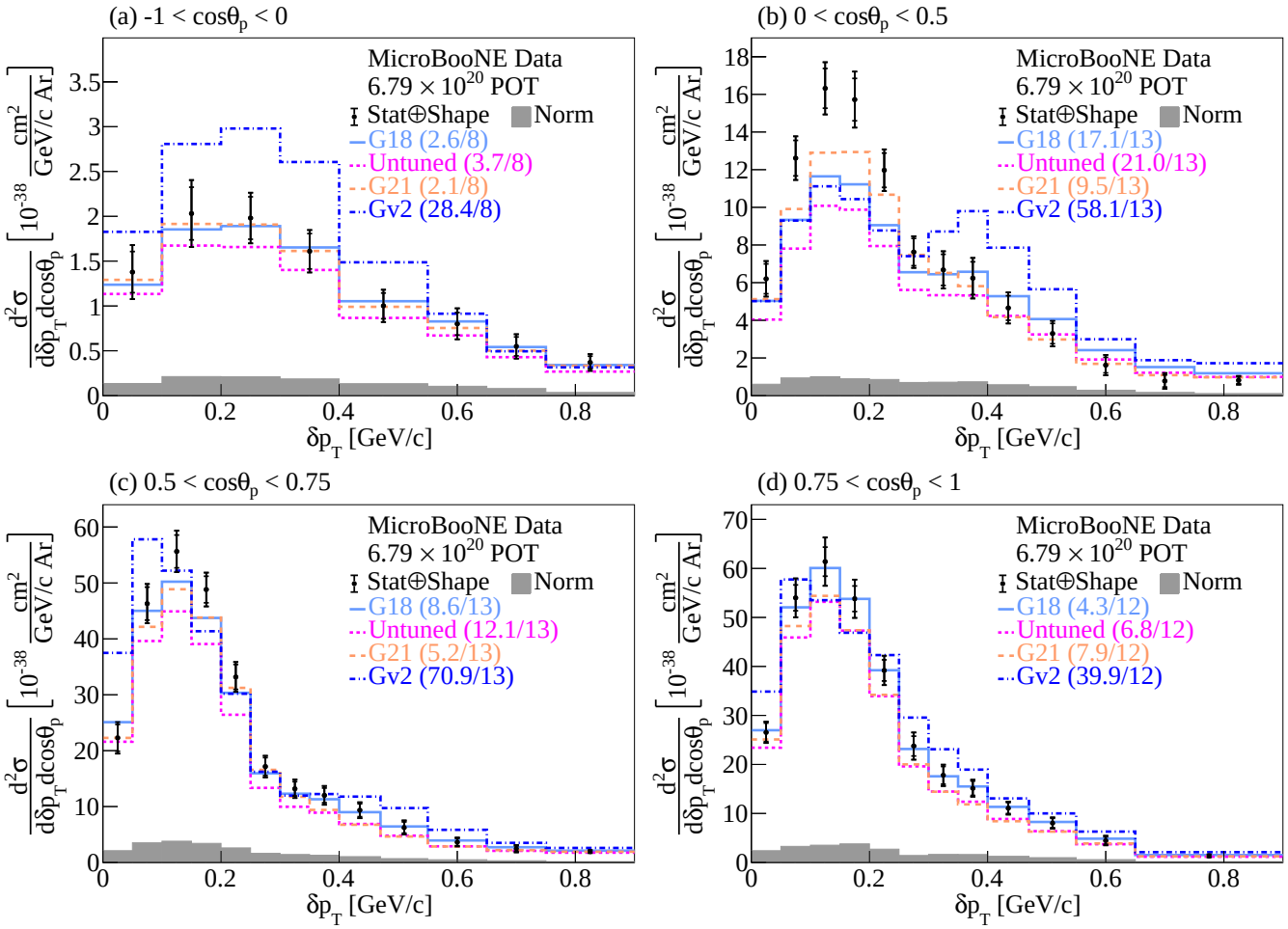

FIG. 16. The flux-integrated double-differential cross sections as a function of δp_T in $\cos\theta_p$ bins. Inner and outer error bars show the statistical and total (statistical and shape systematic) uncertainty at the 1σ, or 68%, confidence level. The gray band shows the normalization systematic uncertainty. Colored lines show the results of theoretical cross section calculations using the `G18` (light blue), `Untuned` (magenta), `G21` (orange), and `Gv2` (dark blue) `GENIE` configurations. The numbers in parentheses show the χ^2/bins calculation for each one of the predictions.

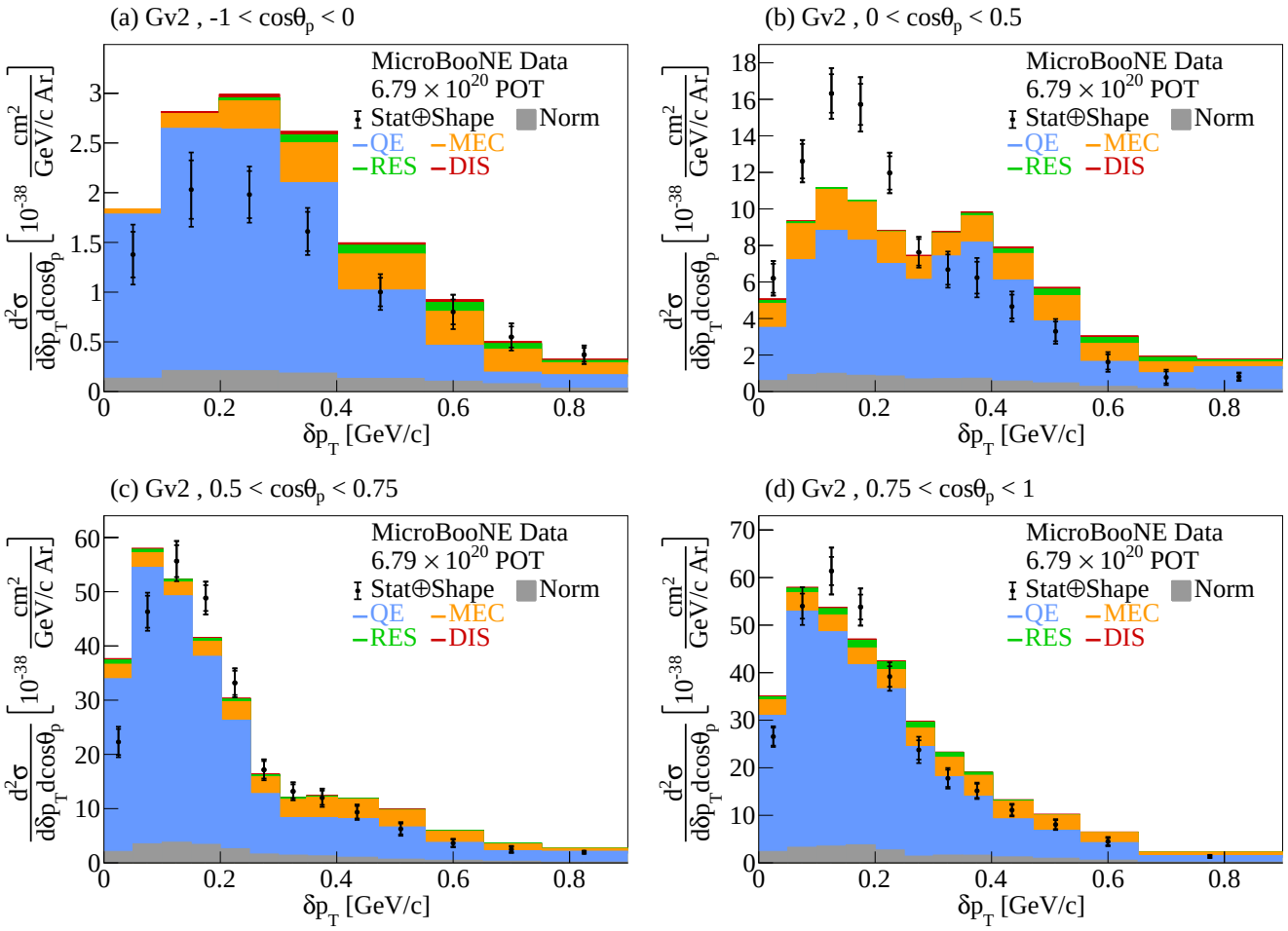

FIG. 17. Comparison between the flux-integrated double-differential cross sections as a function of δp_T for data and the Gv2 GENIE prediction in $\cos\theta_p$ bins. Inner and outer error bars show the statistical and total (statistical and shape systematic) uncertainty at the 1σ, or 68%, confidence level. The gray band shows the normalization systematic uncertainty. Colored stacked histograms show the results of theoretical cross section calculations using the `Gv2 GENIE` prediction for QE (blue), MEC (orange), RES (green), and DIS (red) interactions.

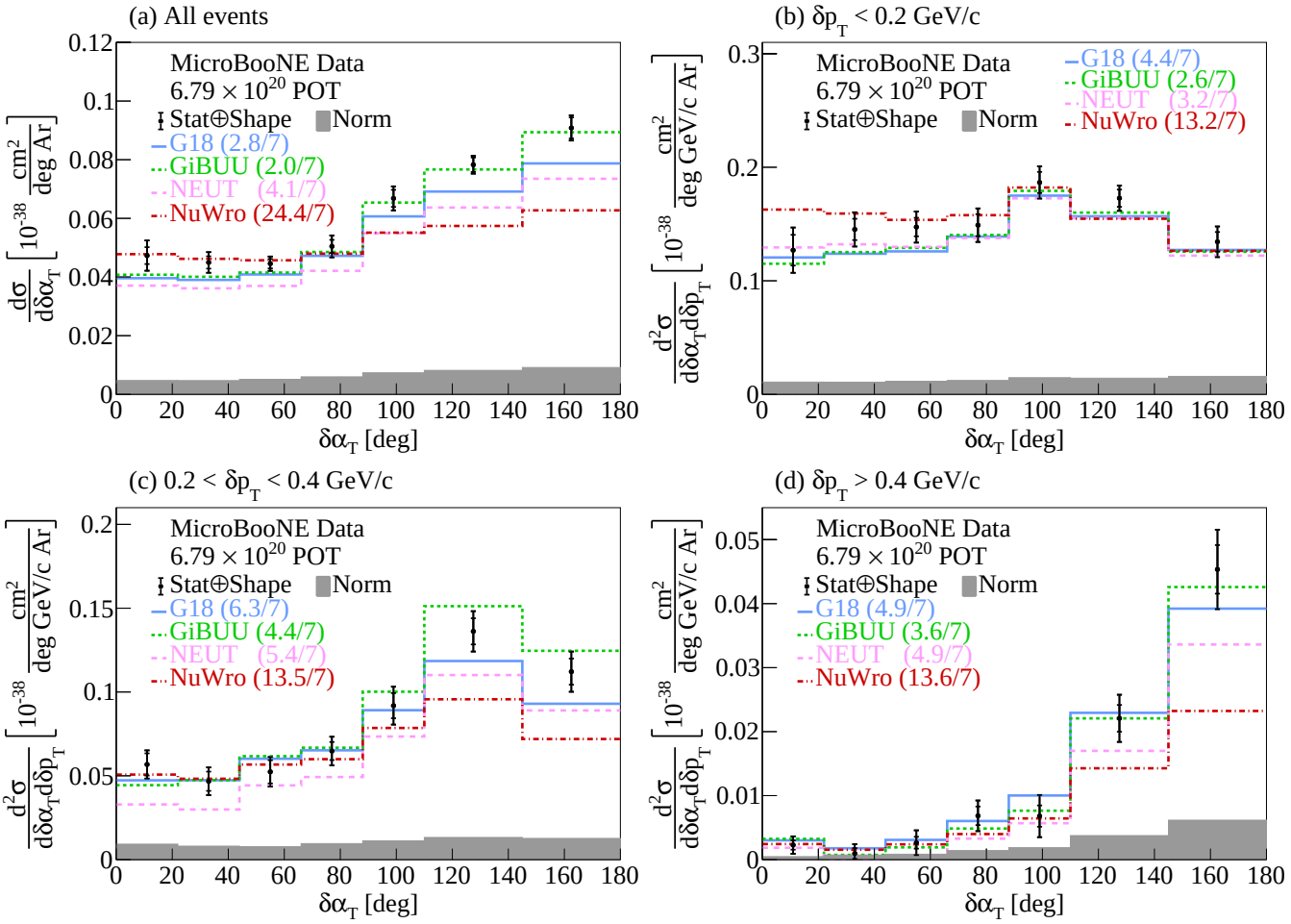

FIG. 18. The flux-integrated (a) single- and (b-d) double- (in δp_T bins) differential cross sections as a function of $\delta\alpha_T$. Inner and outer error bars show the statistical and total (statistical and shape systematic) uncertainty at the 1σ, or 68%, confidence level. The gray band shows the normalization systematic uncertainty. Colored lines show the results of theoretical cross section calculations using the `G18 GENIE` (blue), `GiBUU` (green), `NEUT` (pink), and `NuWro` (red) event generators. The numbers in parentheses show the χ^2/bins calculation for each one of the predictions.

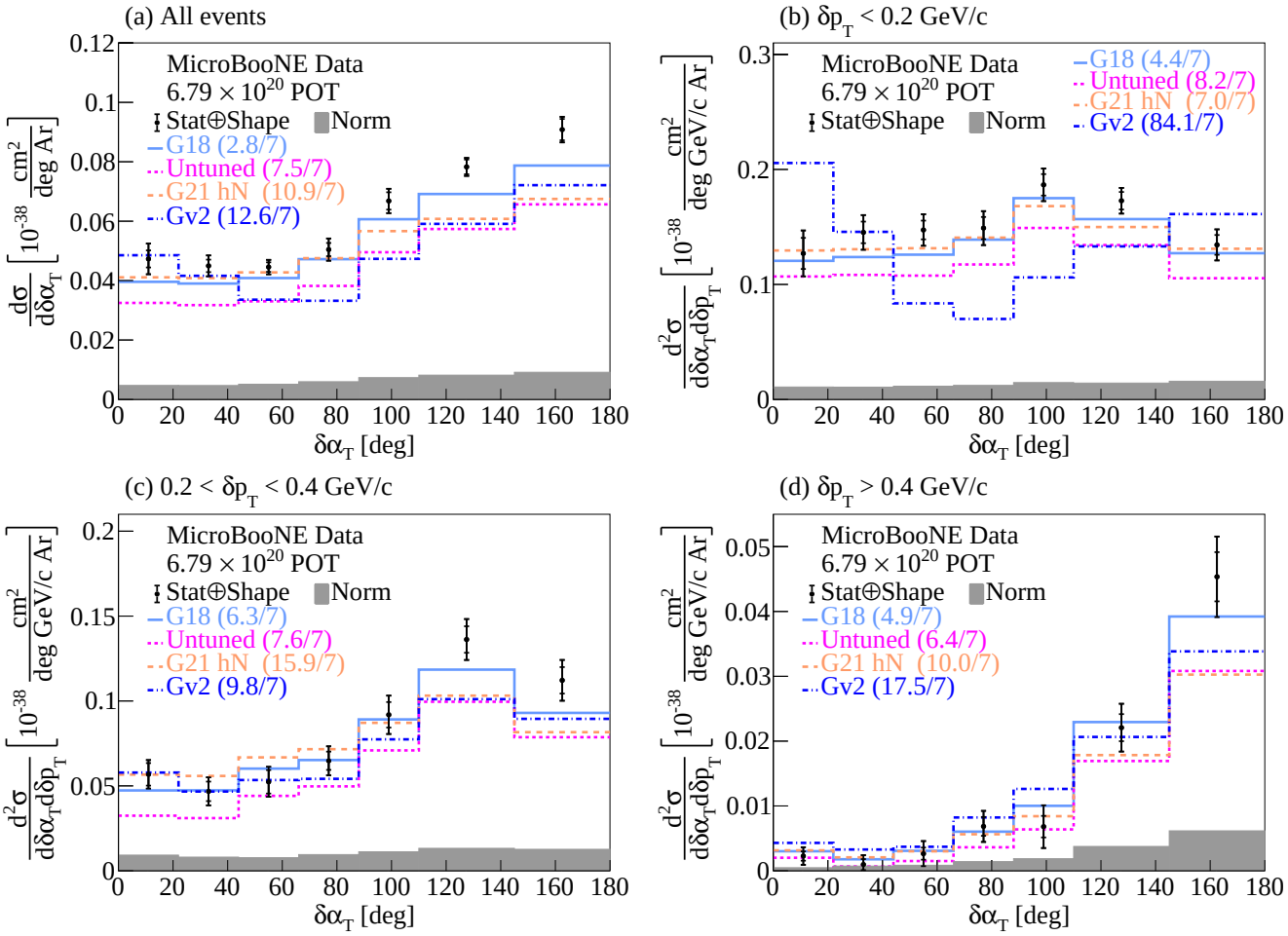

FIG. 19. The flux-integrated (a) single- and (b-d) double- (in δp_T bins) differential cross sections as a function of $\delta\alpha_T$. Inner and outer error bars show the statistical and total (statistical and shape systematic) uncertainty at the 1σ, or 68%, confidence level. The gray band shows the normalization systematic uncertainty. Colored lines show the results of theoretical cross section calculations using the `G18` (light blue), `Untuned` (magenta), `G21` (orange), and `Gv2` (dark blue) `GENIE` configurations. The numbers in parentheses show the χ^2/bins calculation for each one of the predictions.

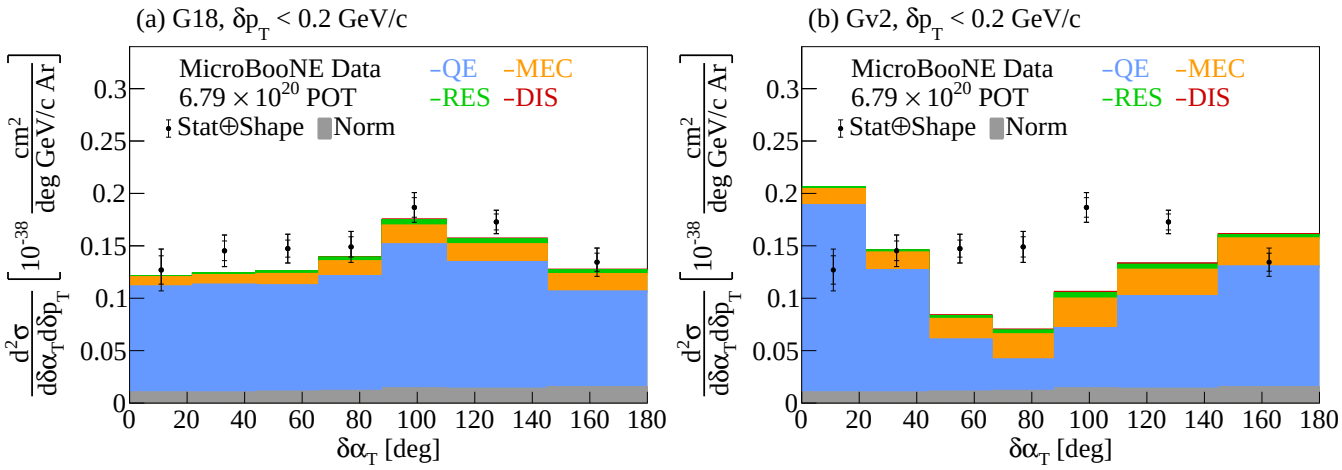

FIG. 20. Comparison between the data flux-integrated double-differential cross section as a function of $\delta\alpha_T$ for events in the region $\delta p_T < 0.2\,\mathrm{GeV}/c$ region against the `G18` and `Gv2 GENIE` predictions. Inner and outer error bars show the statistical and total (statistical and shape systematic) uncertainty at the 1σ, or 68%, confidence level. The gray band shows the normalization systematic uncertainty. Colored stacked histograms show the results of theoretical cross section calculations using the (a) `G18` and (b) `Gv2 GENIE` predictions for QE (blue), MEC (orange), RES (green), and DIS (red) interactions.

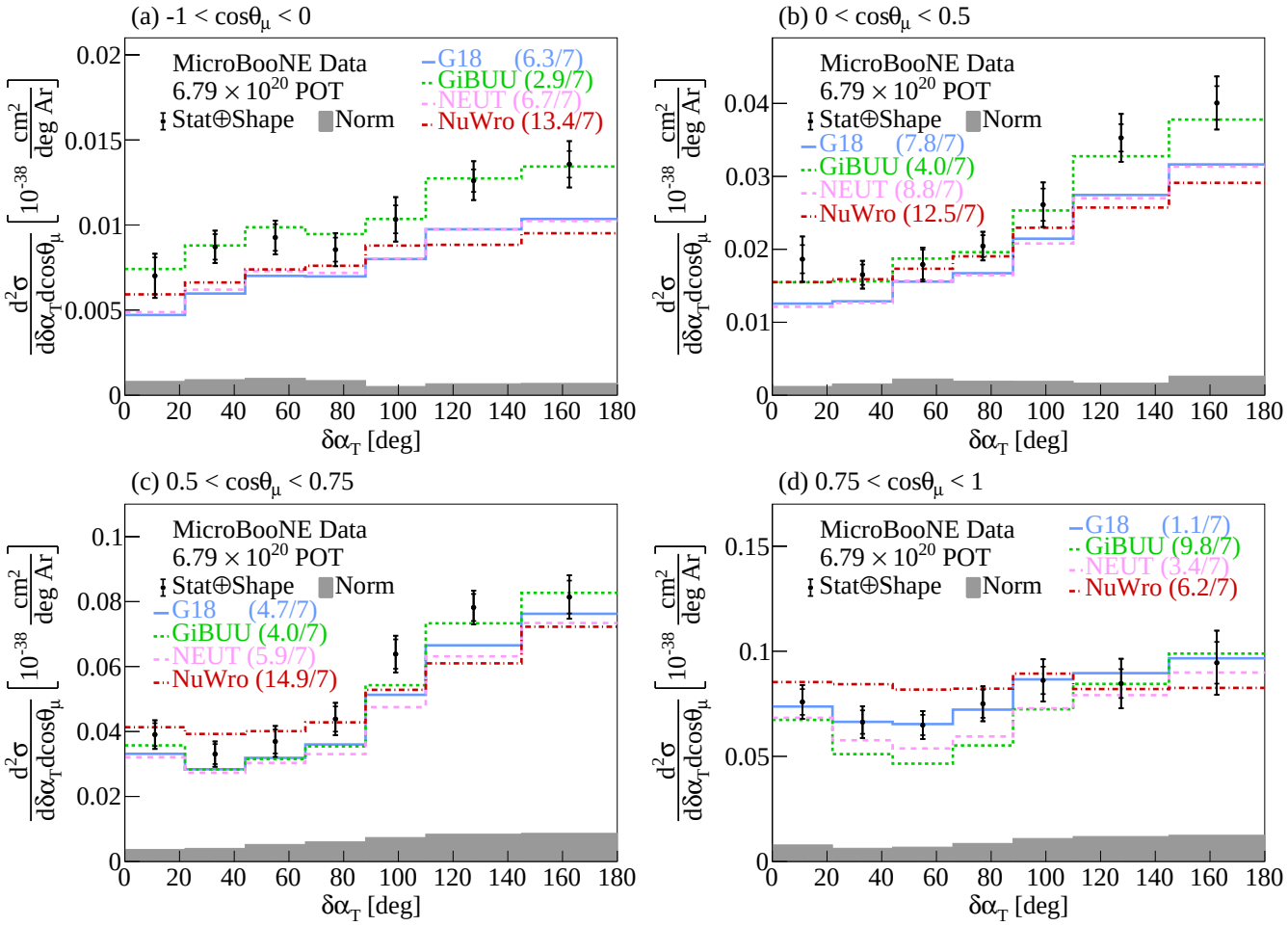

FIG. 21. The flux-integrated double-differential cross sections as a function of $\delta\alpha_T$ in $\cos\theta_\mu$ bins. Inner and outer error bars show the statistical and total (statistical and shape systematic) uncertainty at the 1σ, or 68%, confidence level. The gray band shows the normalization systematic uncertainty. Colored lines show the results of theoretical cross section calculations using the `G18 GENIE` (blue), `GiBUU` (green), `NEUT` (pink), and `NuWro` (red) event generators. The numbers in parentheses show the χ^2/bins calculation for each one of the predictions.

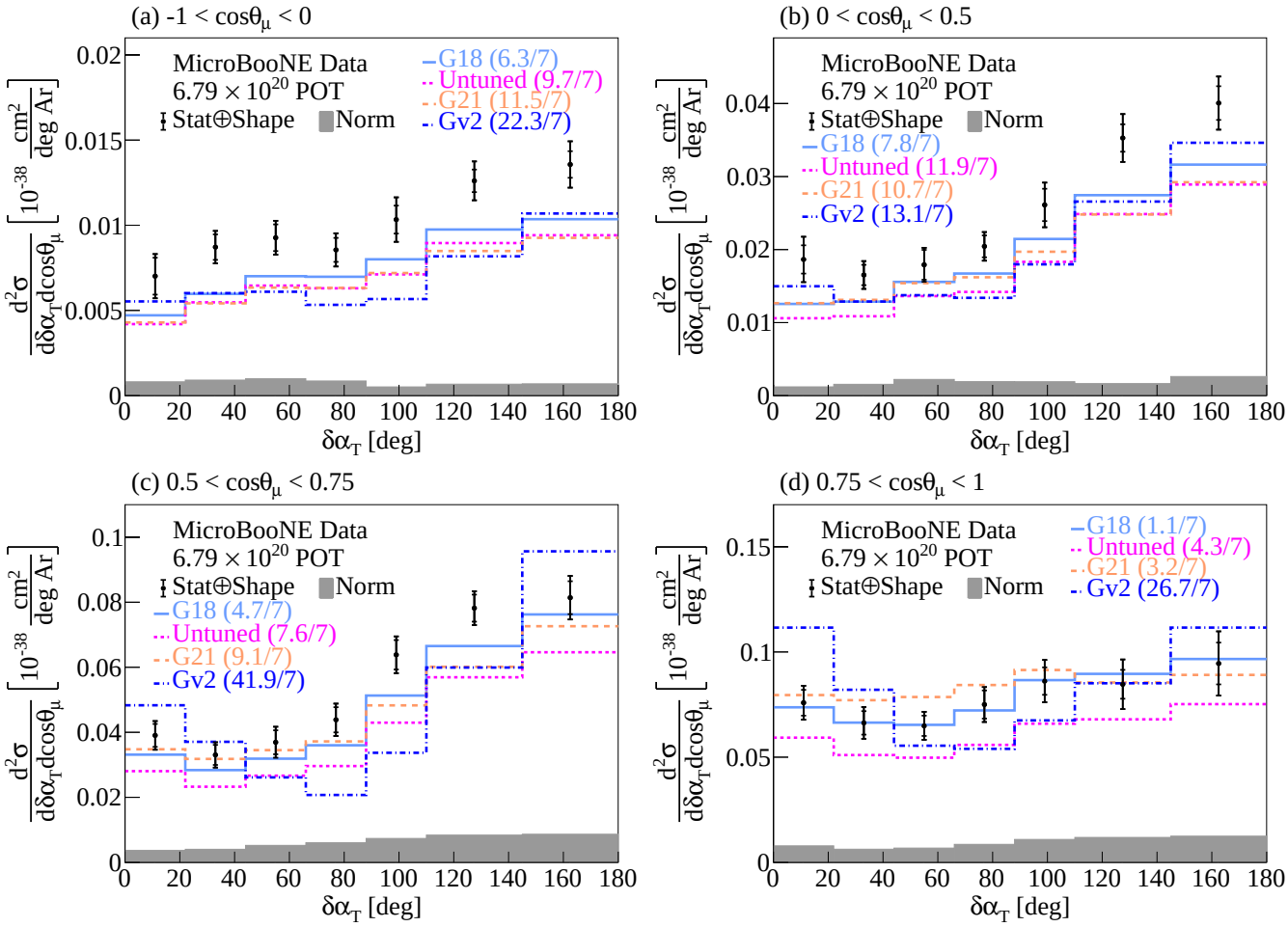

FIG. 22. The flux-integrated double-differential cross sections as a function of $\delta\alpha_T$ in $\cos\theta_\mu$ bins. Inner and outer error bars show the statistical and total (statistical and shape systematic) uncertainty at the 1σ, or 68%, confidence level. The gray band shows the normalization systematic uncertainty. Colored lines show the results of theoretical cross section calculations using the `G18` (light blue), `Untuned` (magenta), `G21` (orange), and `Gv2` (dark blue) `GENIE` configurations. The numbers in parentheses show the χ^2/bins calculation for each one of the predictions.

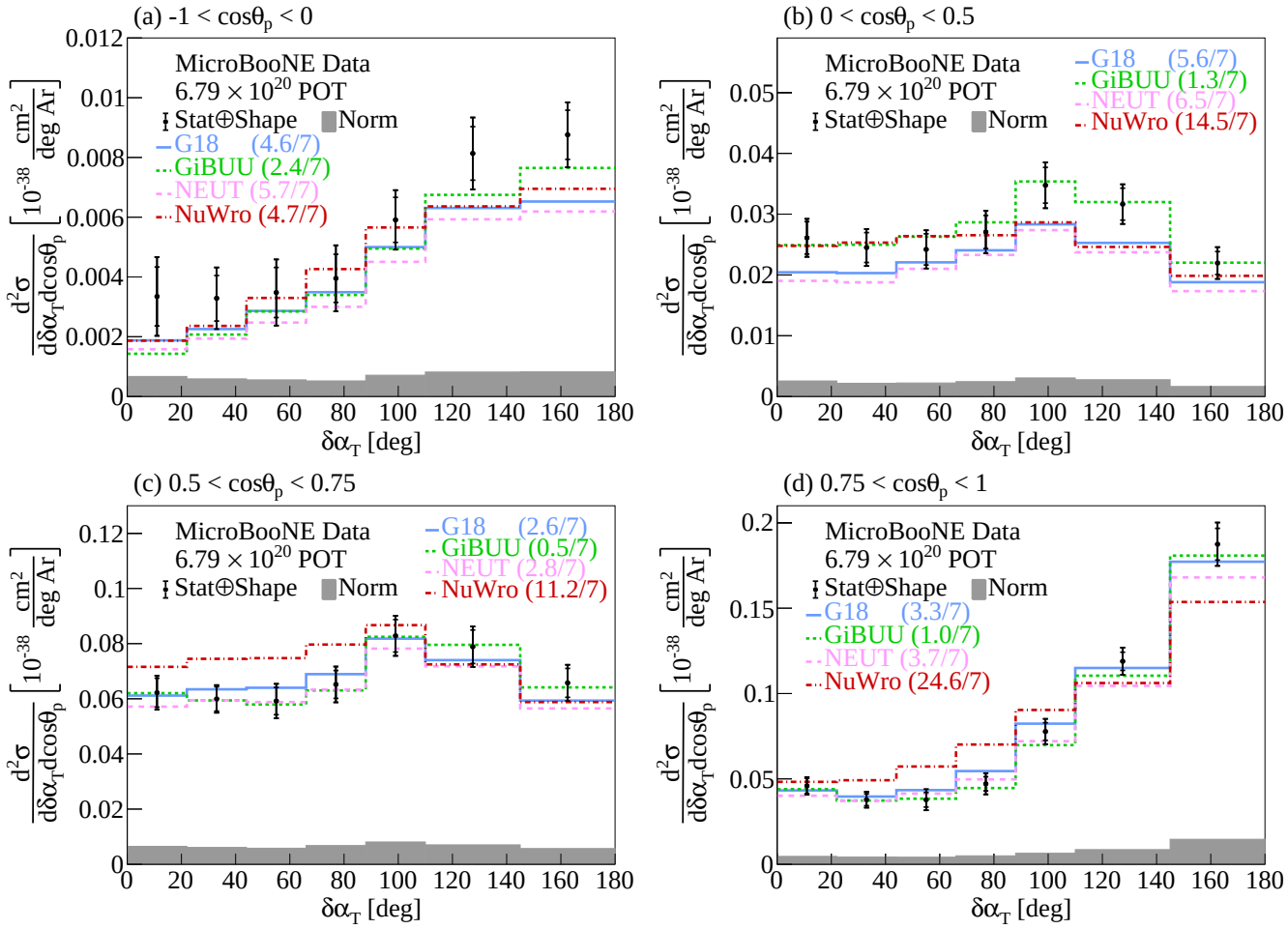

FIG. 23. The flux-integrated double-differential cross sections as a function of $\delta\alpha_T$ in $\cos\theta_p$ bins. Inner and outer error bars show the statistical and total (statistical and shape systematic) uncertainty at the 1σ, or 68%, confidence level. The gray band shows the normalization systematic uncertainty. Colored lines show the results of theoretical cross section calculations using the `G18 GENIE` (blue), `GiBUU` (green), `NEUT` (pink), and `NuWro` (red) event generators. The numbers in parentheses show the χ^2/bins calculation for each one of the predictions.

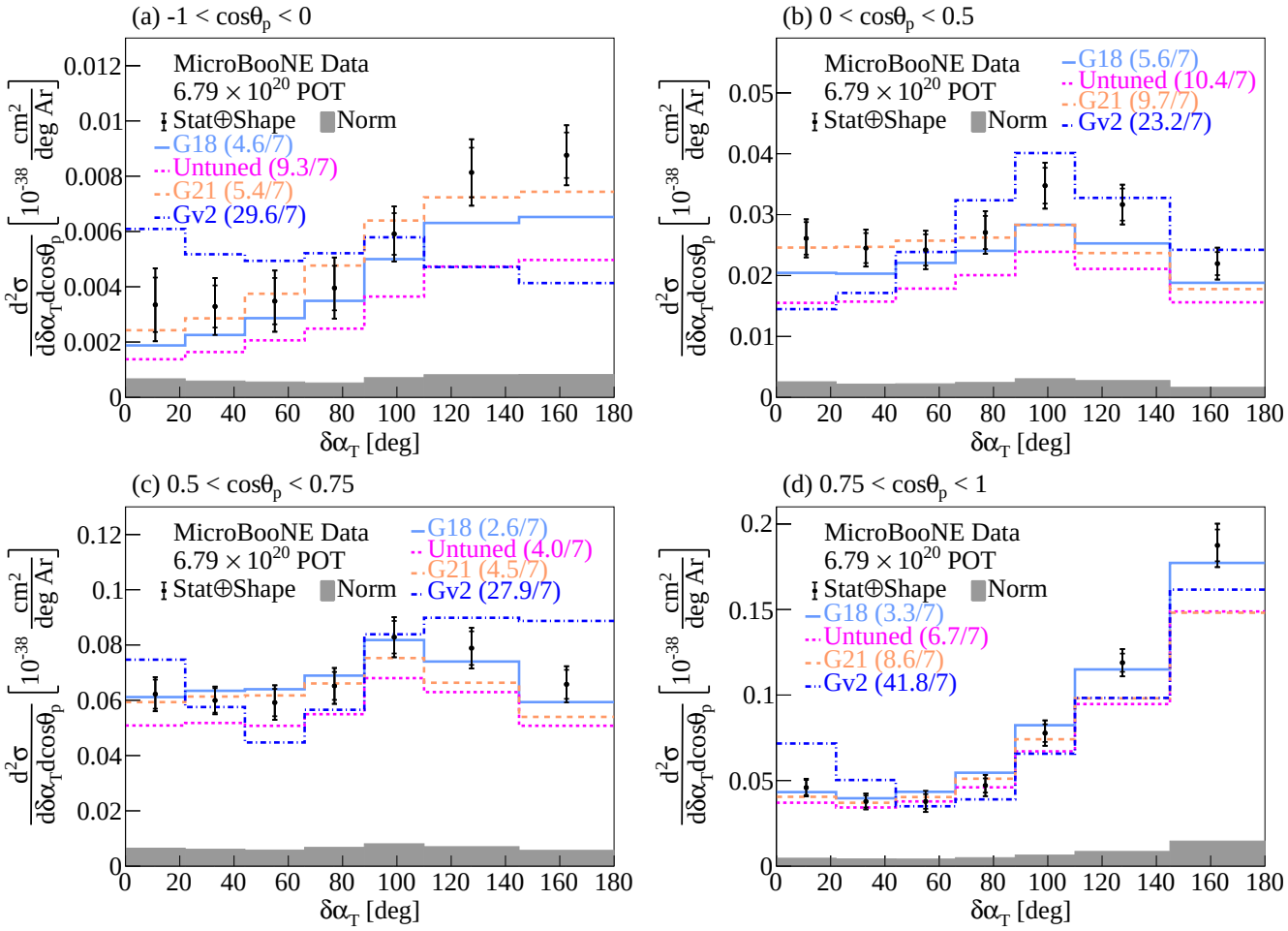

FIG. 24. The flux-integrated double-differential cross sections as a function of $\delta\alpha_T$ in $\cos\theta_p$ bins. Inner and outer error bars show the statistical and total (statistical and shape systematic) uncertainty at the 1σ, or 68%, confidence level. The gray band shows the normalization systematic uncertainty. Colored lines show the results of theoretical cross section calculations using the `G18` (light blue), `Untuned` (magenta), `G21` (orange), and `Gv2` (dark blue) `GENIE` configurations. The numbers in parentheses show the χ^2/bins calculation for each one of the predictions.

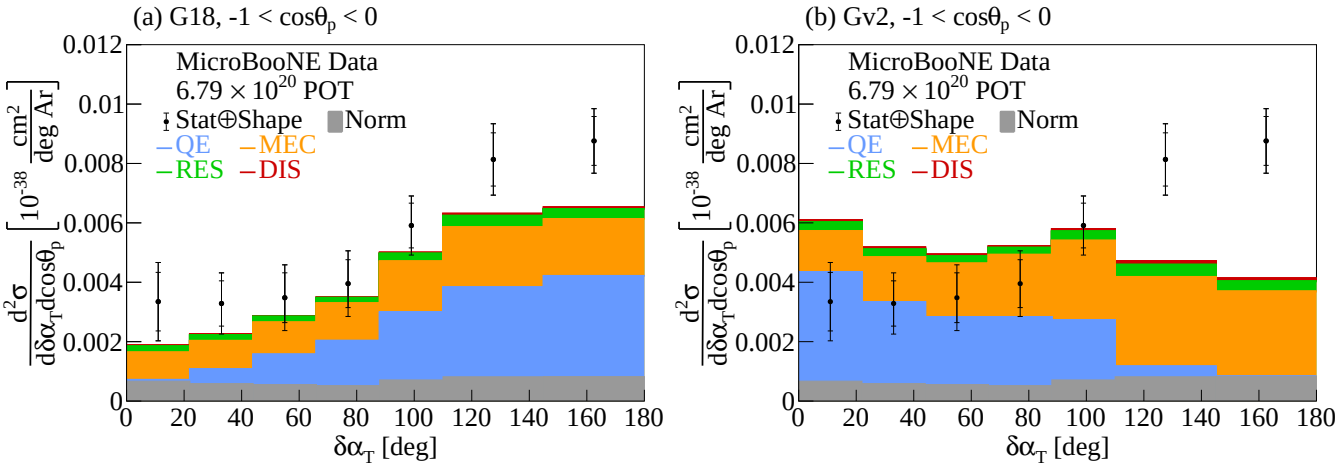

FIG. 25. Comparison between the data flux-integrated double-differential cross section as a function of $\delta\alpha_T$ for events in the region -1 < $\cos\theta_p$ < 0 region against the `G18` and `Gv2 GENIE` predictions. Inner and outer error bars show the statistical and total (statistical and shape systematic) uncertainty at the 1σ, or 68%, confidence level. The gray band shows the normalization systematic uncertainty. Colored stacked histograms show the results of theoretical cross section calculations using the (a) `G18` and (b) `Gv2 GENIE` predictions for QE (blue), MEC (orange), RES (green), and DIS (red) interactions.

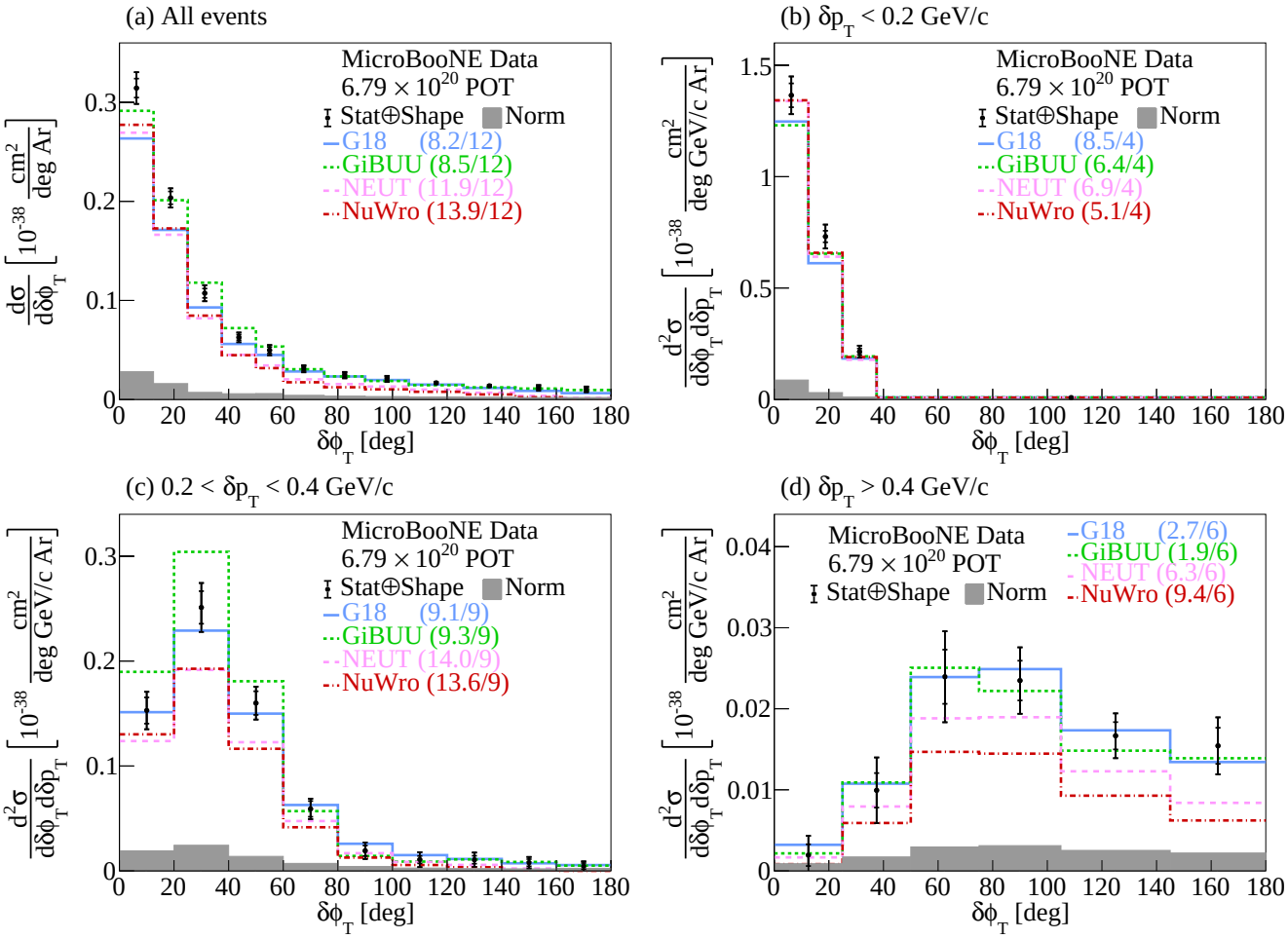

FIG. 26. The flux-integrated (a) single- and (b-d) double- (in δp_T bins) differential cross sections as a function of $\delta\phi_T$. Inner and outer error bars show the statistical and total (statistical and shape systematic) uncertainty at the 1σ, or 68%, confidence level. The gray band shows the normalization systematic uncertainty. Colored lines show the results of theoretical cross section calculations using the `G18 GENIE` (blue), `GiBUU` (green), `NEUT` (pink), and `NuWro` (red) event generators. The numbers in parentheses show the χ^2/bins calculation for each one of the predictions.

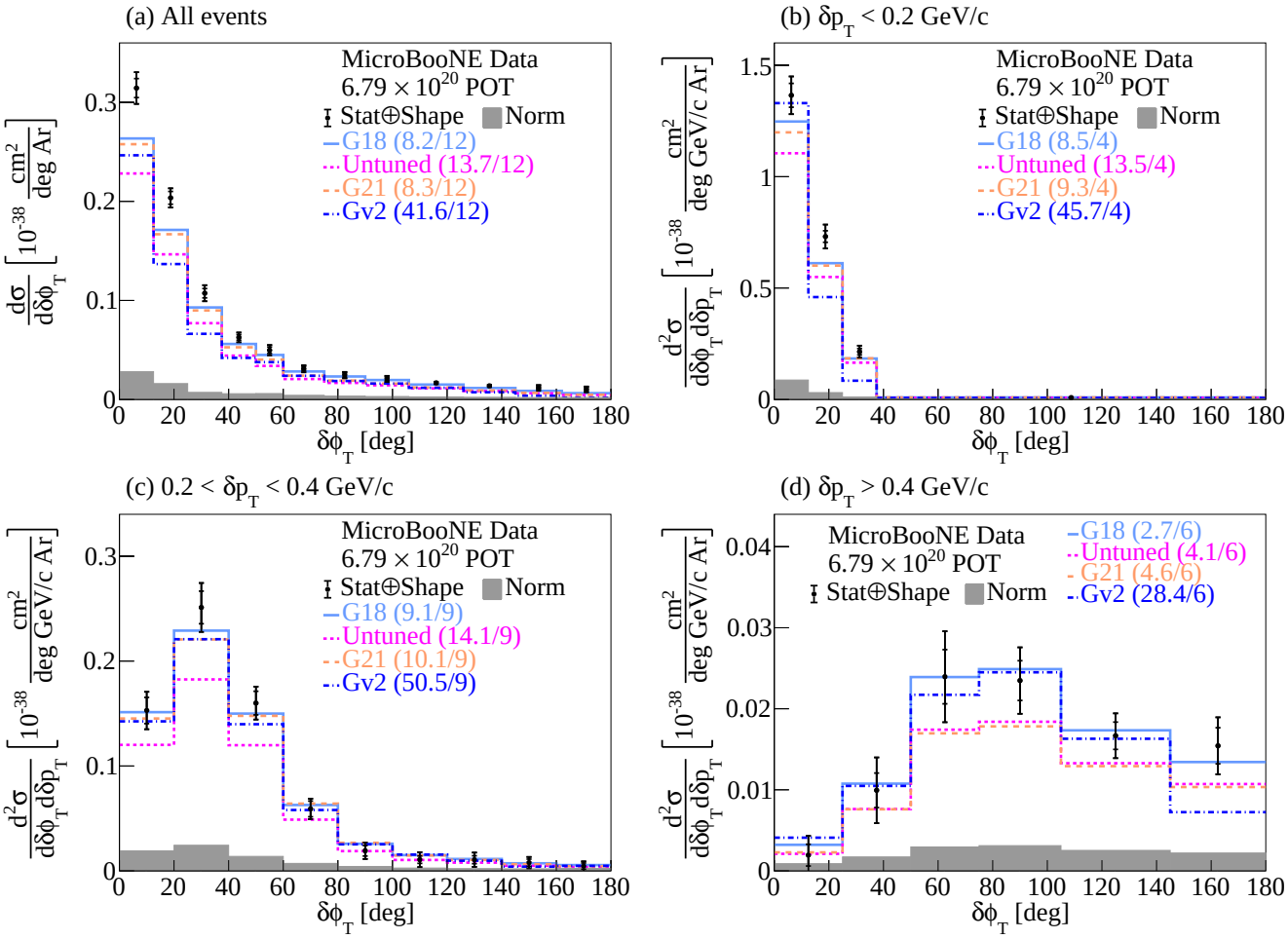

FIG. 27. The flux-integrated (a) single- and (b-d) double- (in δp_T bins) differential cross sections as a function of $\delta\phi_T$. Inner and outer error bars show the statistical and total (statistical and shape systematic) uncertainty at the 1σ, or 68%, confidence level. The gray band shows the normalization systematic uncertainty. Colored lines show the results of theoretical cross section calculations using the `G18` (light blue), `Untuned` (magenta), `G21` (orange), and `Gv2` (dark blue) `GENIE` configurations. The numbers in parentheses show the χ^2/bins calculation for each one of the predictions.

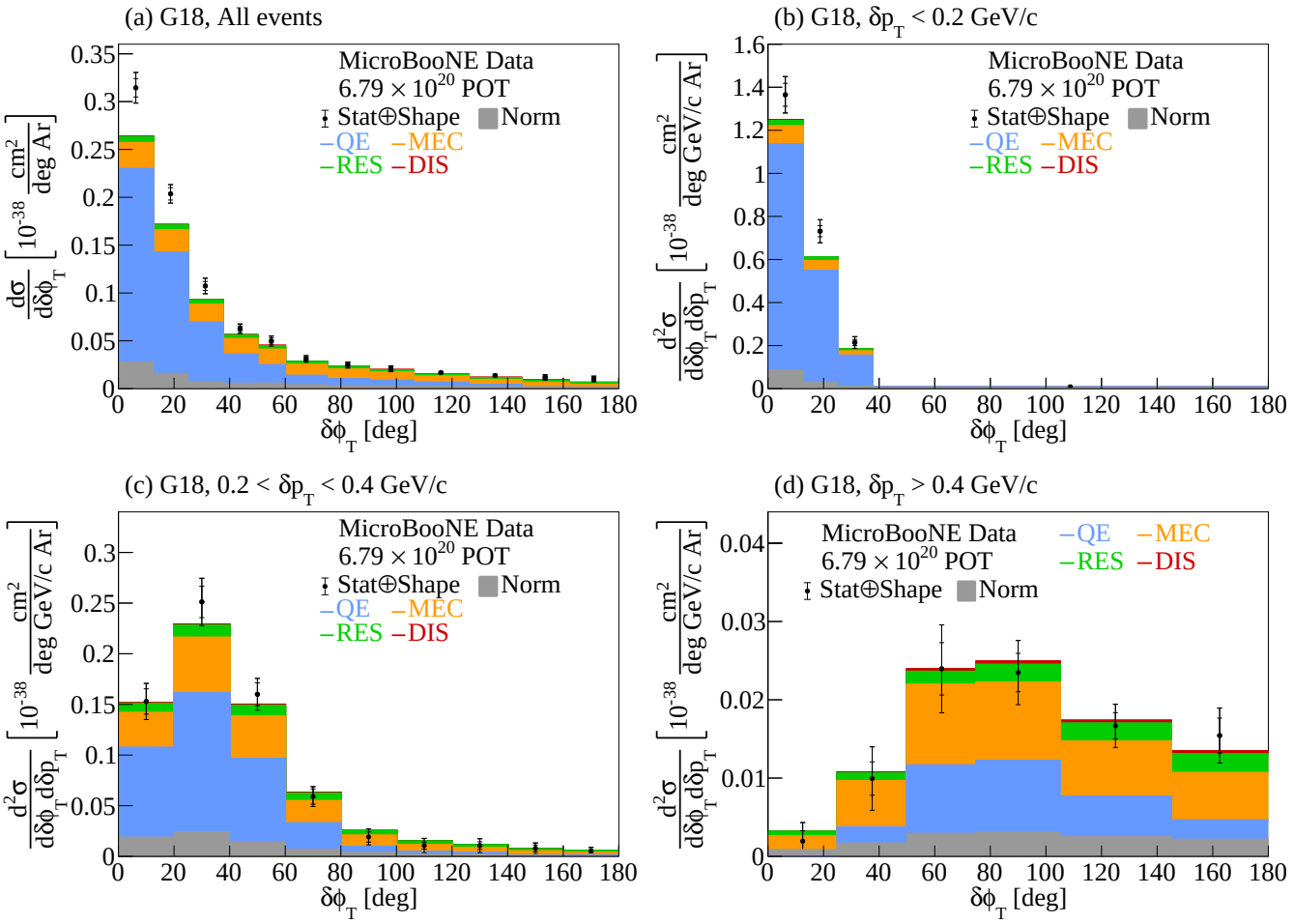

FIG. 28. Comparison between the flux-integrated double- (in δp_T bins) differential cross sections as a function of $\delta\phi_T$ for data and the `G18 GENIE` prediction. Inner and outer error bars show the statistical and total (statistical and shape systematic) uncertainty at the 1σ, or 68%, confidence level. The gray band shows the normalization systematic uncertainty. Colored stacked histograms show the results of theoretical cross section calculations using the `G18` prediction for QE (blue), MEC (orange), RES (green), and DIS (red) interactions.

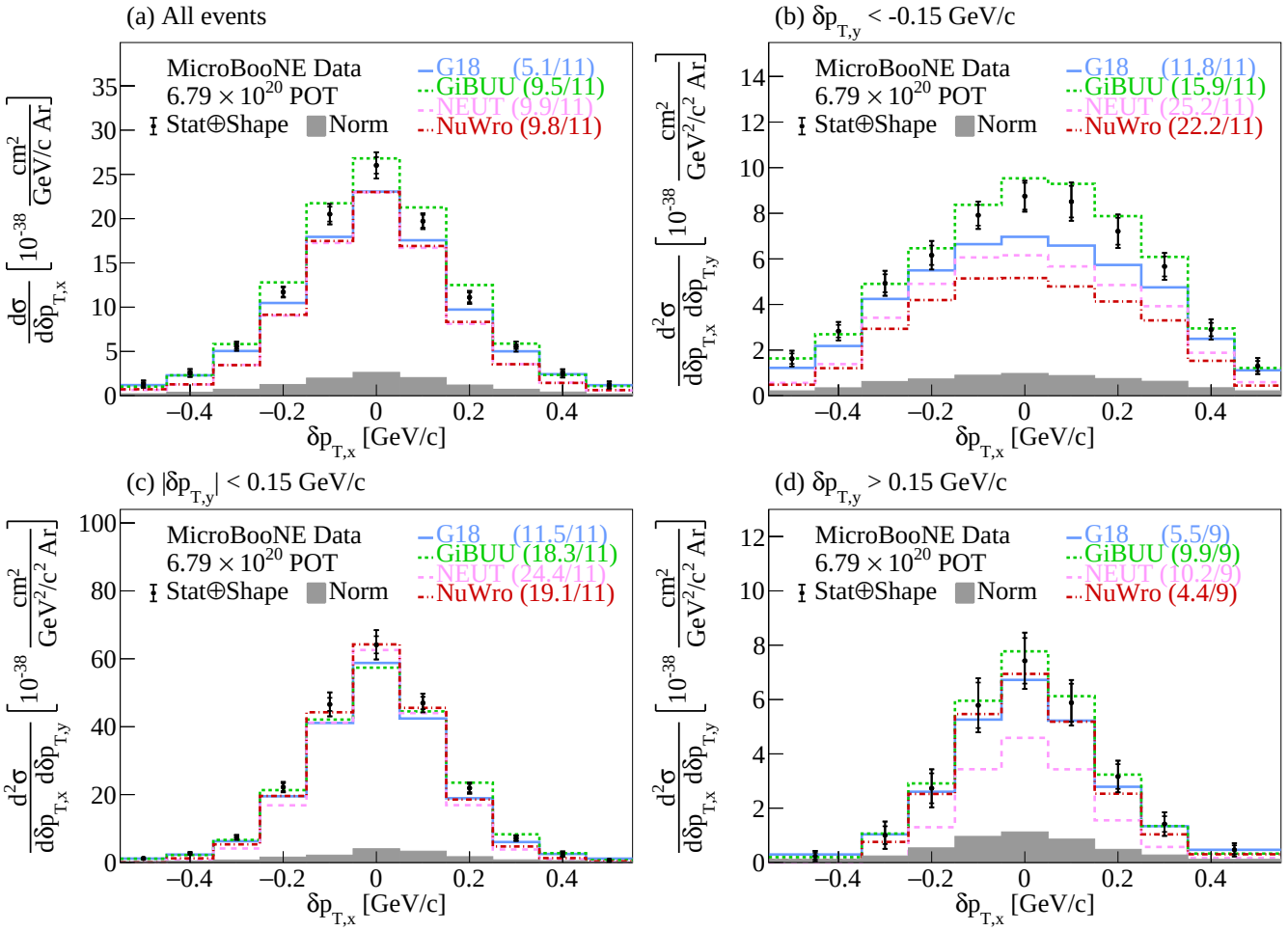

FIG. 29. The flux-integrated (a) single- and (b-d) double- (in $\delta p_{T,y}$ bins) differential cross sections as a function of $\delta p_{T,x}$. Inner and outer error bars show the statistical and total (statistical and shape systematic) uncertainty at the 1σ, or 68%, confidence level. The gray band shows the normalization systematic uncertainty. Colored lines show the results of theoretical cross section calculations using the `G18 GENIE` (blue), `GiBUU` (green), `NEUT` (pink), and `NuWro` (red) event generators. The numbers in parentheses show the χ^2/bins calculation for each one of the predictions.

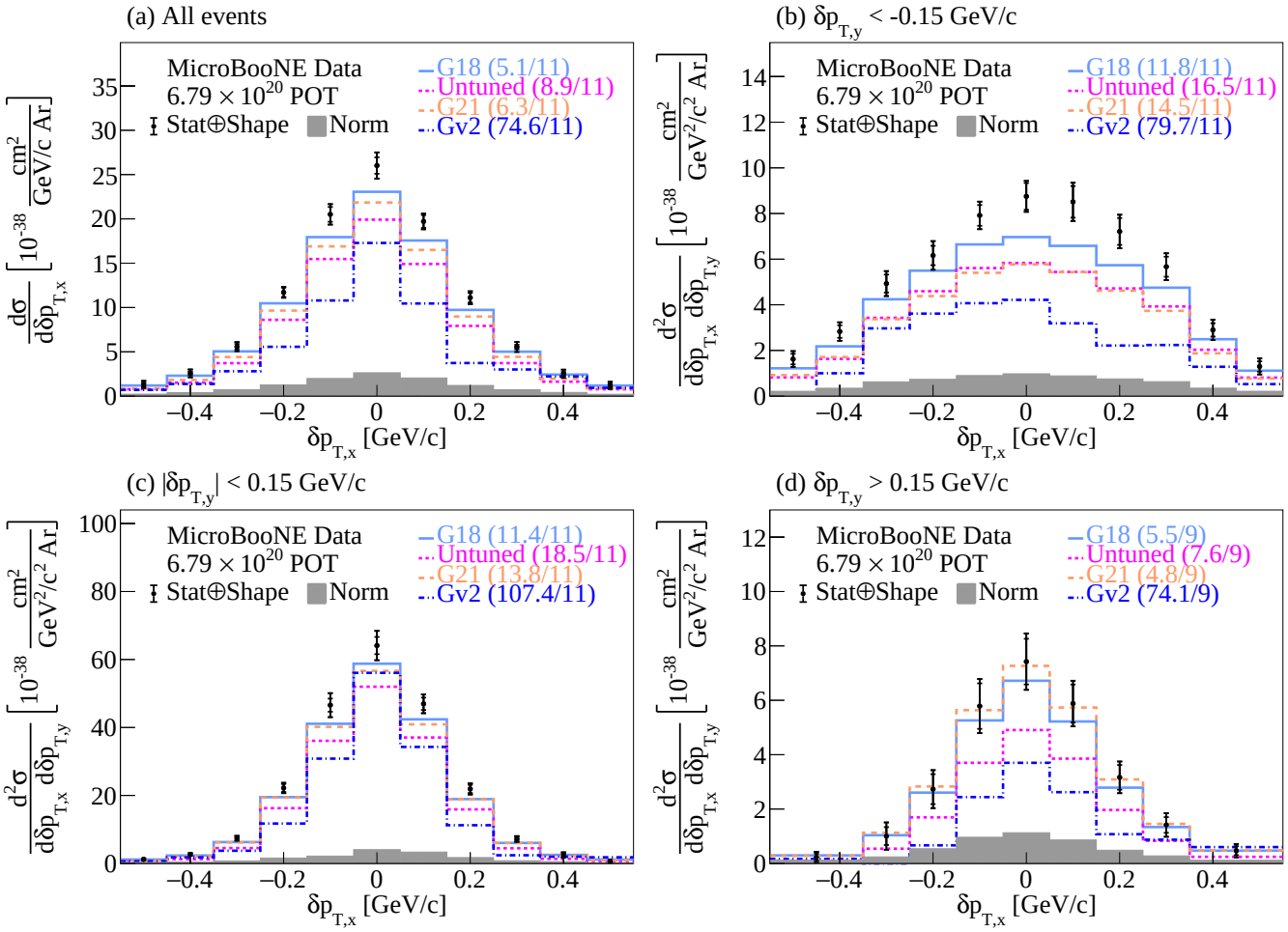

FIG. 30. The flux-integrated (a) single- and (b-d) double- (in $\delta p_{T,y}$ bins) differential cross sections as a function of $\delta p_{T,x}$. Inner and outer error bars show the statistical and total (statistical and shape systematic) uncertainty at the 1σ, or 68%, confidence level. The gray band shows the normalization systematic uncertainty. Colored lines show the results of theoretical cross section calculations using the `G18` (light blue), `Untuned` (magenta), `G21` (orange), and `Gv2` (dark blue) `GENIE` configurations. The numbers in parentheses show the χ^2/bins calculation for each one of the predictions.

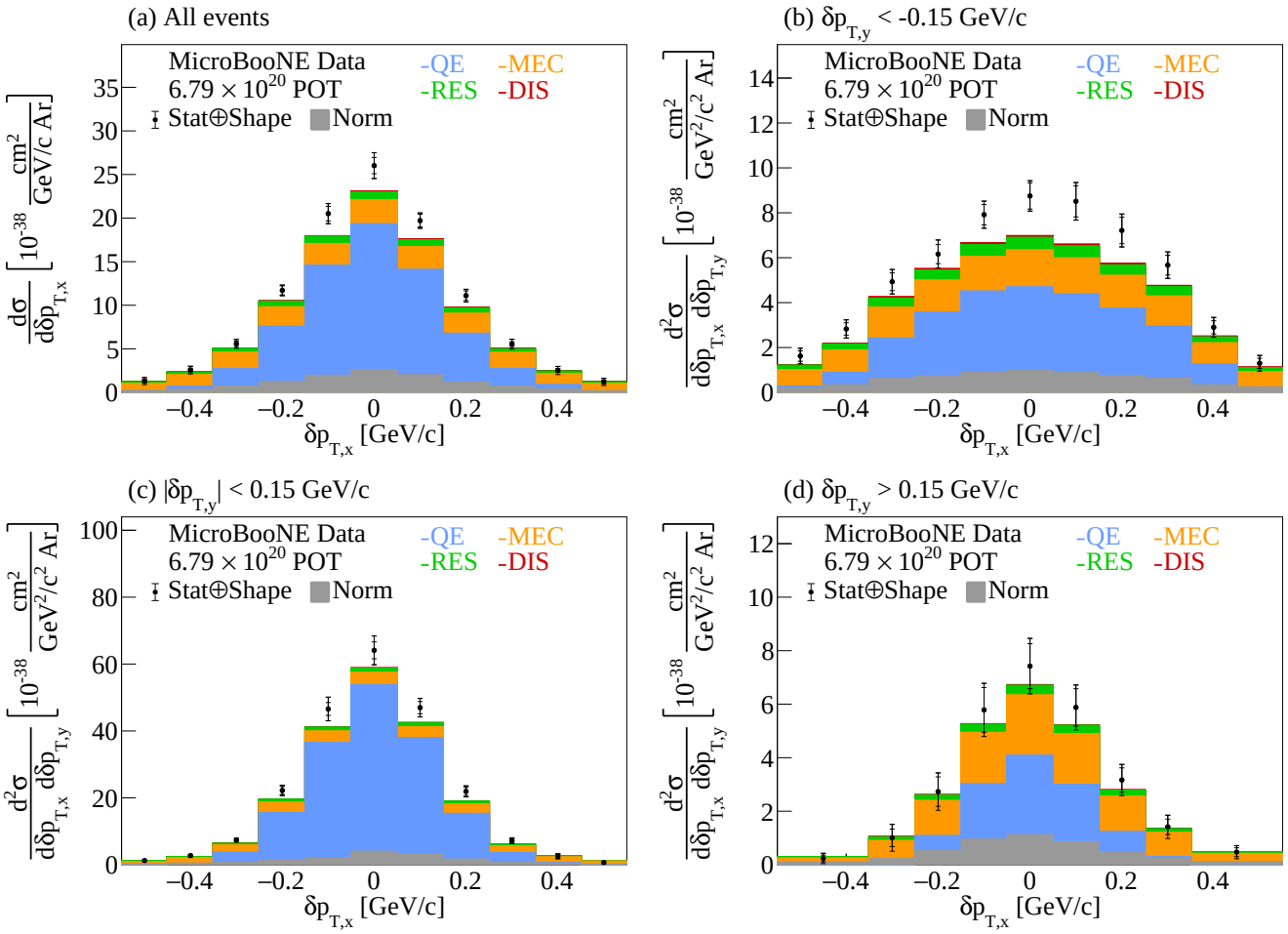

FIG. 31. Comparison between the flux-integrated double- (in $\delta p_{T,y}$ bins) differential cross sections as a function of $\delta p_{T,x}$ for data and the `G18 GENIE` prediction. Inner and outer error bars show the statistical and total (statistical and shape systematic) uncertainty at the 1σ, or 68%, confidence level. The gray band shows the normalization systematic uncertainty. Colored stacked histograms show the results of theoretical cross section calculations using the `G18 GENIE` prediction for QE (blue), MEC (orange), RES (green), and DIS (red) interactions.

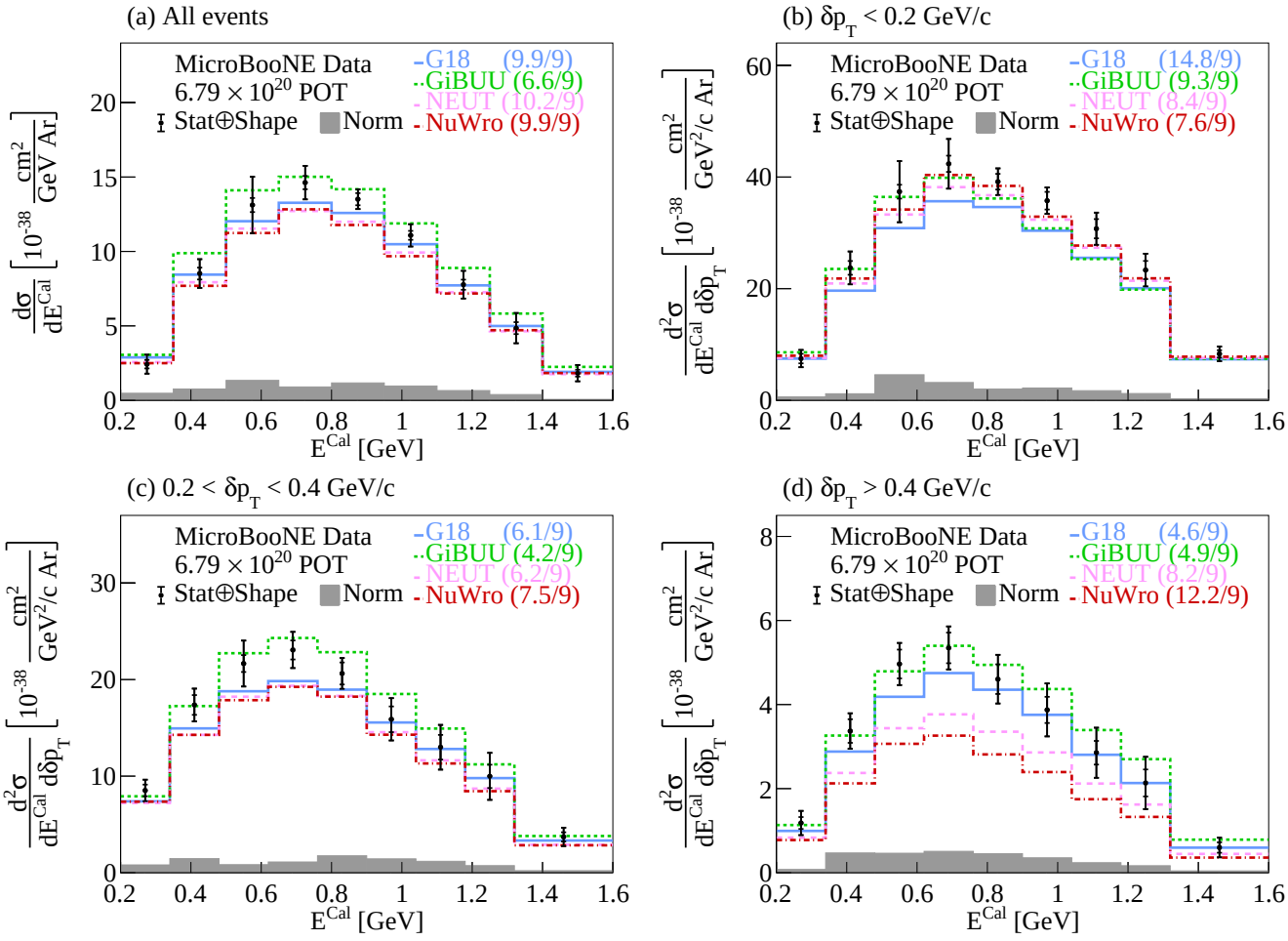

FIG. 32. The flux-integrated (a) single- and (b-d) double- (in δp_T bins) differential cross sections as a function of E^{Cal}. Inner and outer error bars show the statistical and total (statistical and shape systematic) uncertainty at the 1σ, or 68%, confidence level. The gray band shows the normalization systematic uncertainty. Colored lines show the results of theoretical cross section calculations using the `G18 GENIE` (blue), `GiBUU` (green), `NEUT` (pink), and `NuWro` (red) event generators. The numbers in parentheses show the χ^2/bins calculation for each one of the predictions.

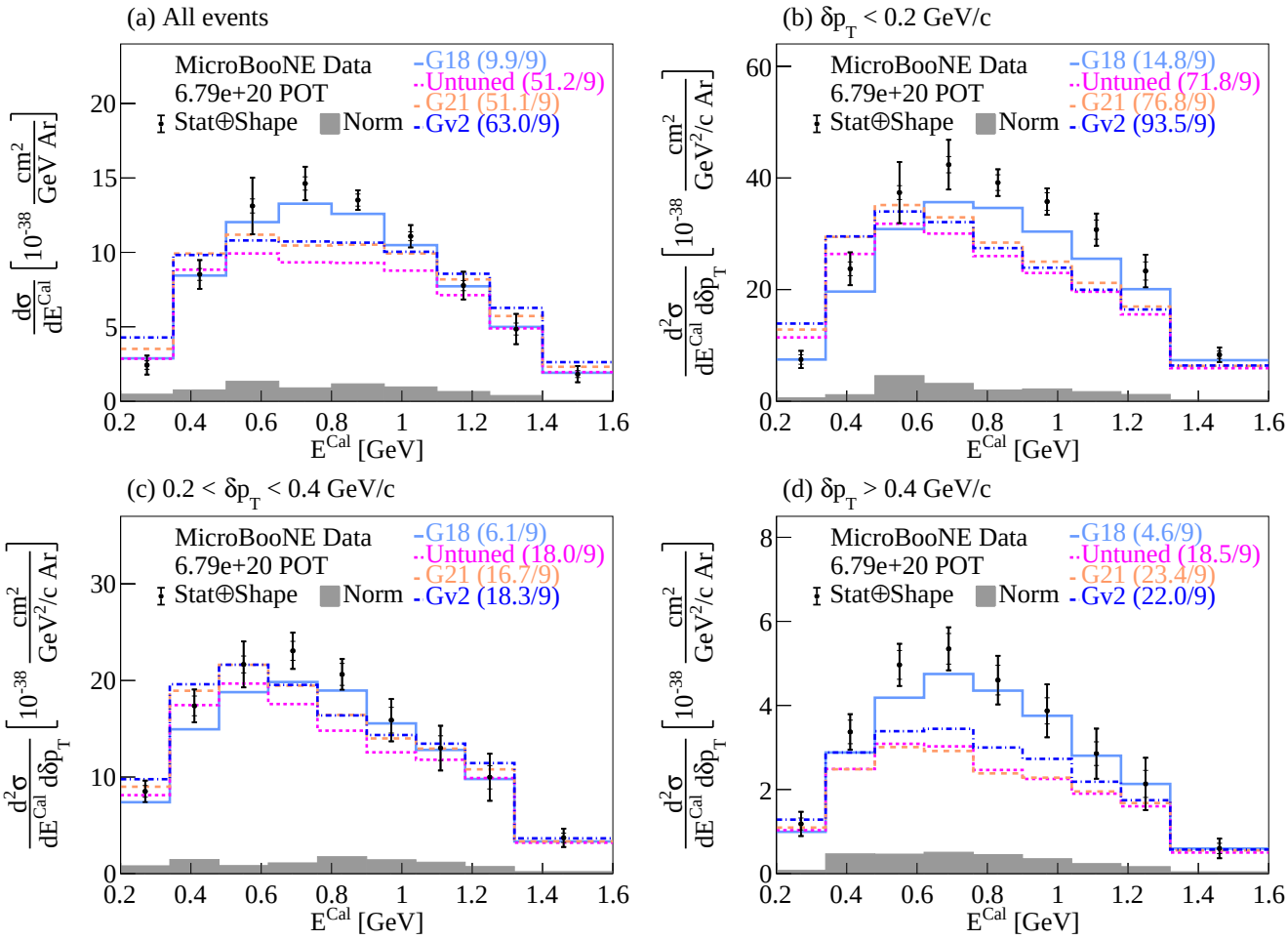

FIG. 33. The flux-integrated (a) single- and (b-d) double- in δp_T bins differential cross sections as a function of E^{Cal}. Inner and outer error bars show the statistical and total (statistical and shape systematic) uncertainty at the 1σ, or 68%, confidence level. The gray band shows the normalization systematic uncertainty. Colored lines show the results of theoretical cross section calculations using the `G18` (light blue), `Untuned` (magenta), `G21` (orange), and `Gv2` (dark blue) `GENIE` configurations.

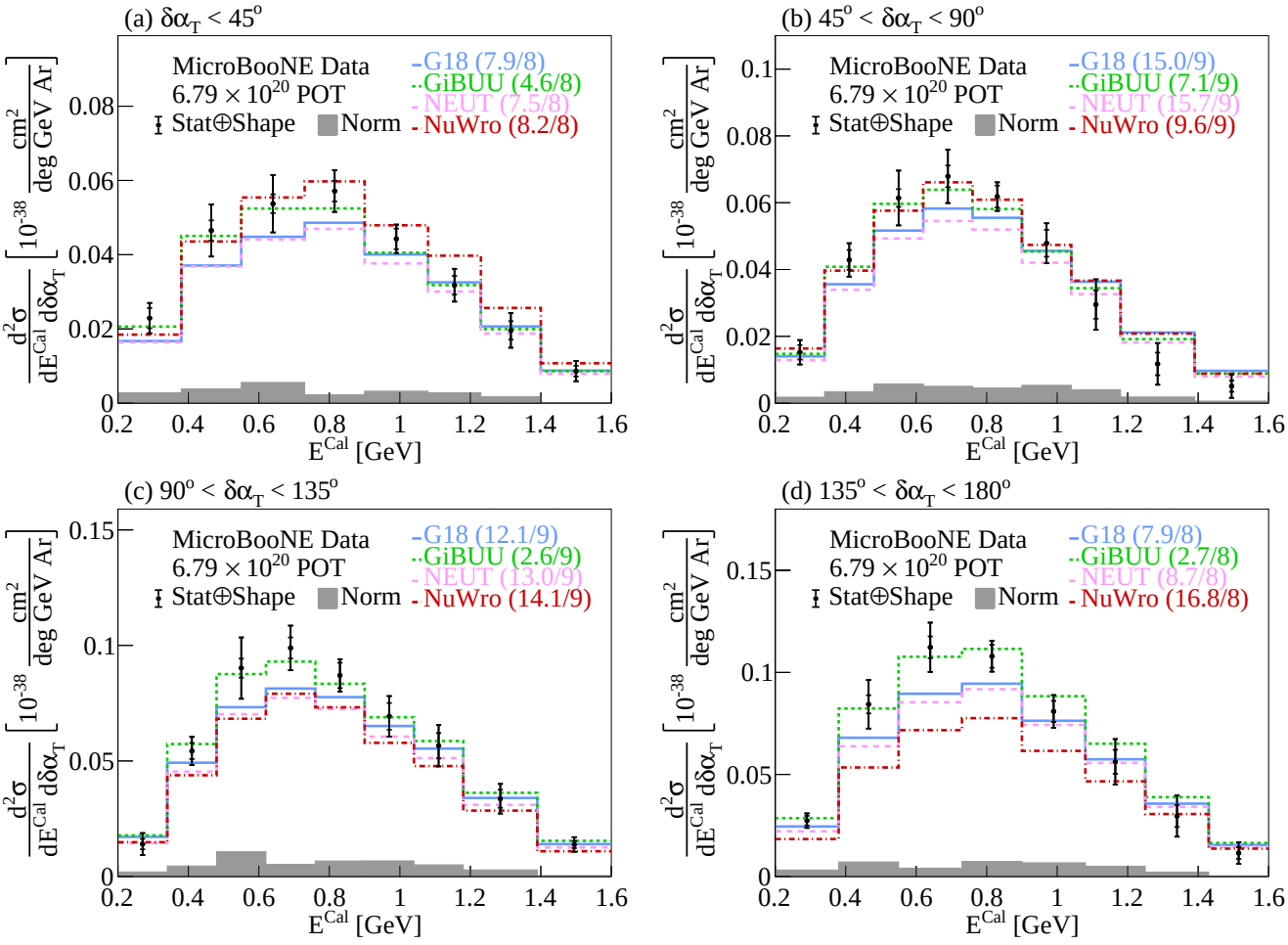

FIG. 34. The flux-integrated double-differential cross sections as a function of E^{Cal} in $\delta\alpha_T$ bins. Inner and outer error bars show the statistical and total (statistical and shape systematic) uncertainty at the 1σ, or 68%, confidence level. The gray band shows the normalization systematic uncertainty. Colored lines show the results of theoretical cross section calculations using the `G18 GENIE` (blue), `GiBUU` (green), `NEUT` (pink), and `NuWro` (red) event generators. The numbers in parentheses show the χ^2/bins calculation for each one of the predictions.

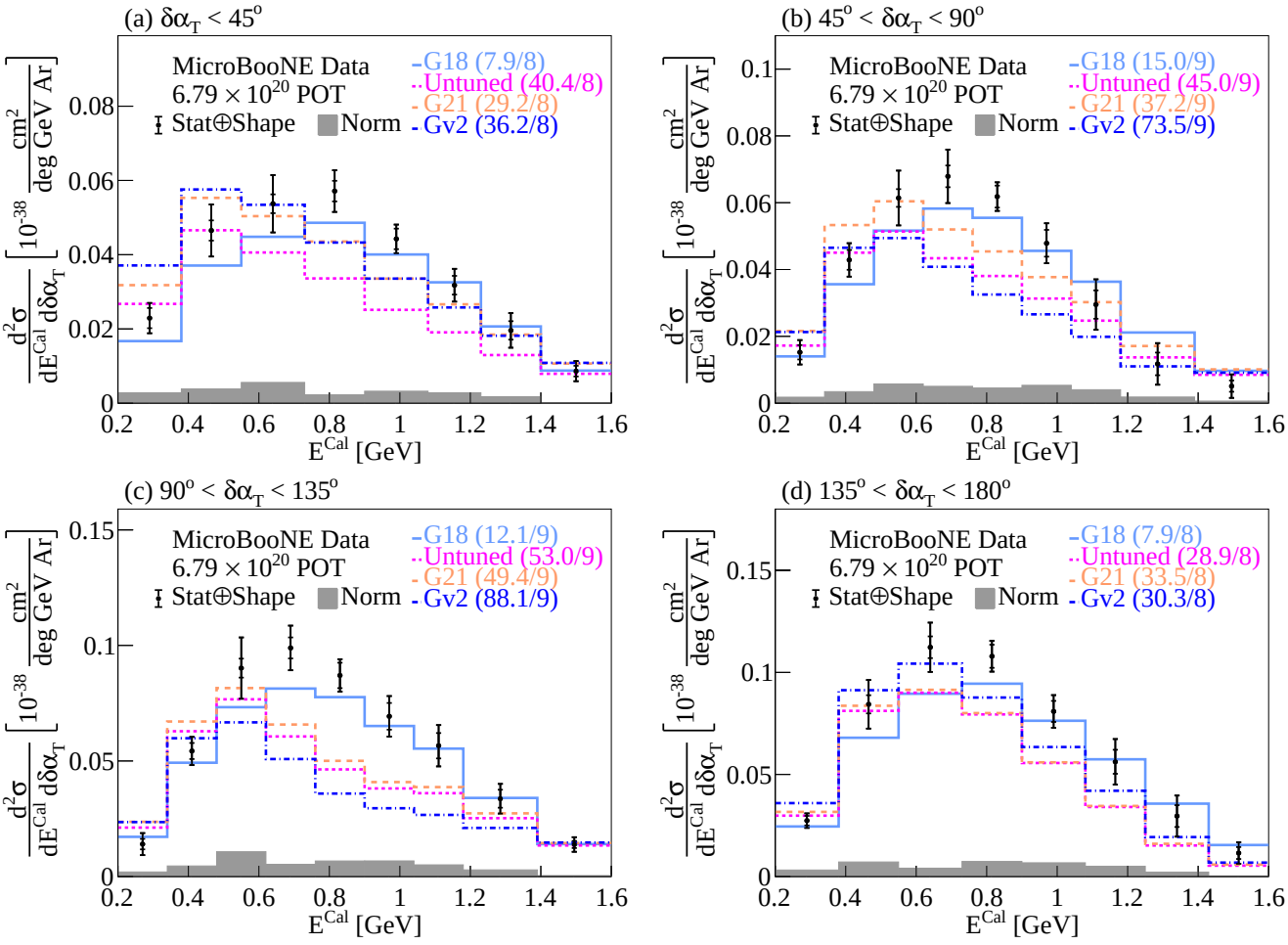

FIG. 35. The flux-integrated double-differential cross sections as a function of E^{Cal} in $\delta\alpha_T$ bins. Inner and outer error bars show the statistical and total (statistical and shape systematic) uncertainty at the 1σ, or 68%, confidence level. The gray band shows the normalization systematic uncertainty. Colored lines show the results of theoretical cross section calculations using the `G18` (light blue), `Untuned` (magenta), `G21` (orange), and `Gv2` (dark blue) `GENIE` configurations. The numbers in parentheses show the χ^2/bins calculation for each one of the predictions.

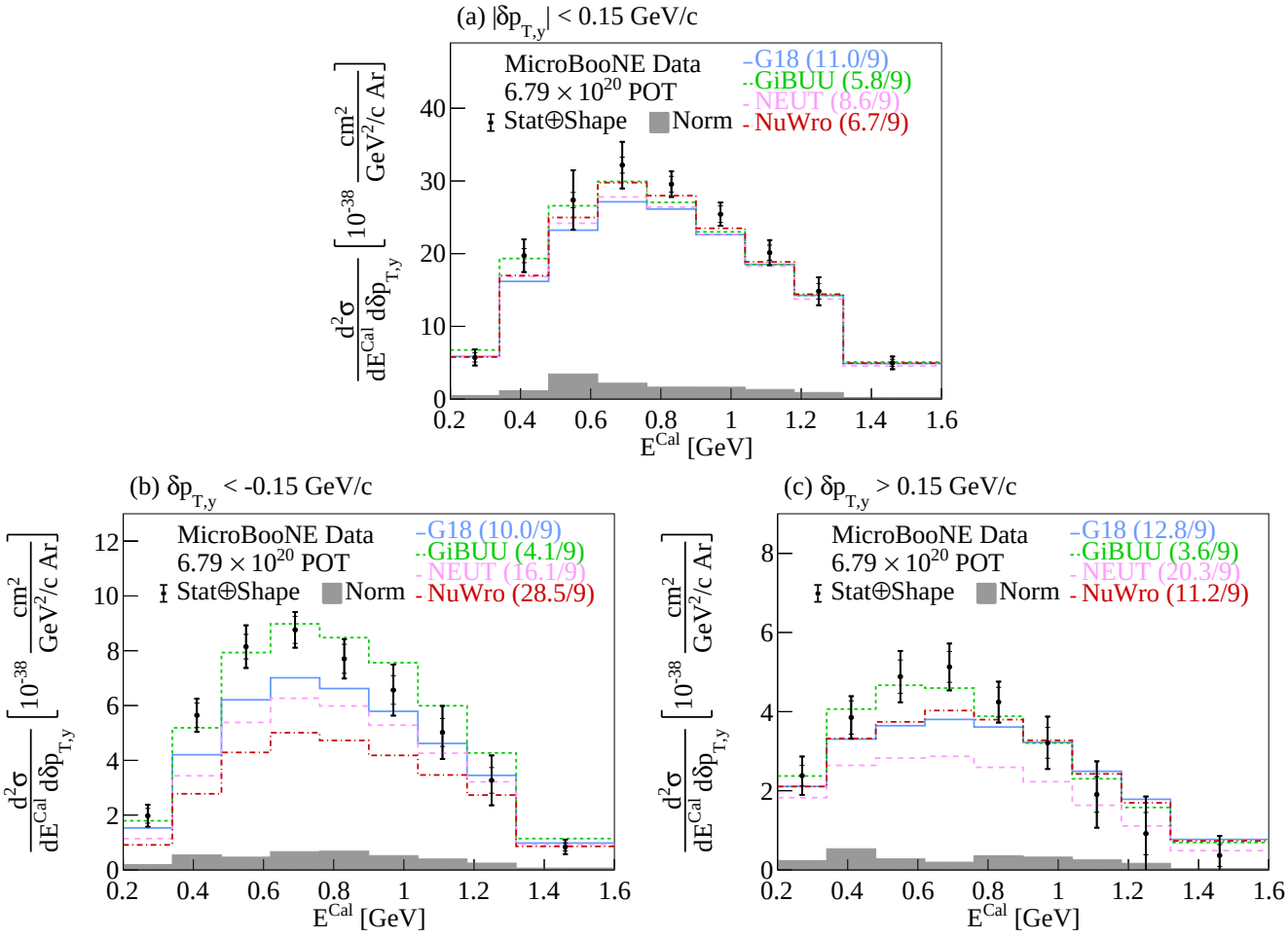

FIG. 36. The flux-integrated double-differential cross sections as a function of E^{Cal} in $\delta p_{T,y}$ bins. Inner and outer error bars show the statistical and total (statistical and shape systematic) uncertainty at the 1σ, or 68%, confidence level. The gray band shows the normalization systematic uncertainty. Colored lines show the results of theoretical cross section calculations using the `G18 GENIE` (blue), `GiBUU` (green), `NEUT` (pink), and `NuWro` (red) event generators. The numbers in parentheses show the χ^2/bins calculation for each one of the predictions.

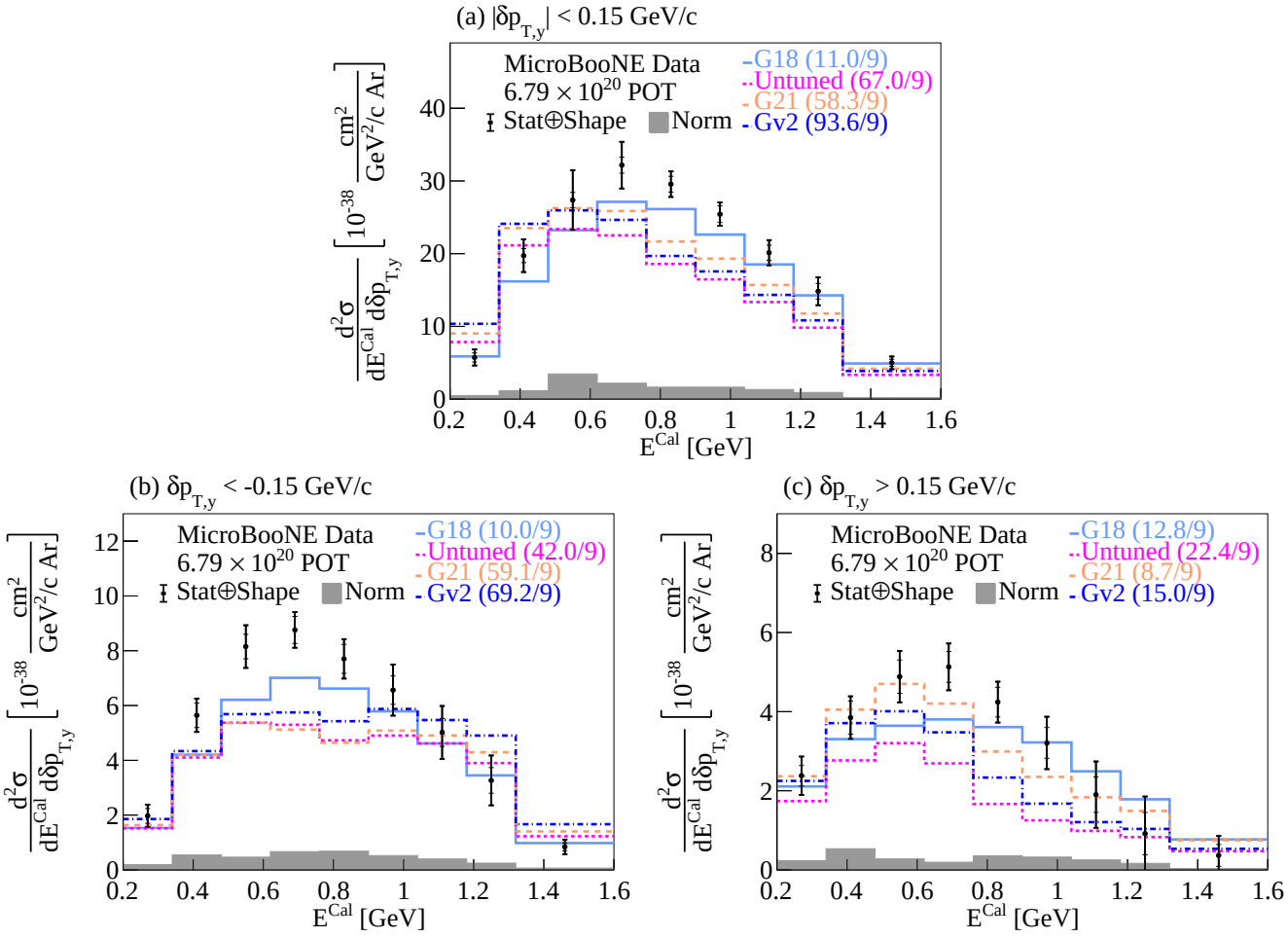

FIG. 37. The flux-integrated double-differential cross sections as a function of E^{Cal} in $\delta p_{T,y}$ bins. Inner and outer error bars show the statistical and total (statistical and shape systematic) uncertainty at the 1σ, or 68%, confidence level. The gray band shows the normalization systematic uncertainty. Colored lines show the results of theoretical cross section calculations using the `G18` (light blue), `Untuned` (magenta), `G21` (orange), and `Gv2` (dark blue) `GENIE` configurations. The numbers in parentheses show the χ^2/bins calculation for each one of the predictions.

[1] M. Tanabashi *et al.* (Particle Data Group), Phys. Rev. D **98**, 030001 (2018).
[2] K. Abe *et al.* (T2K Collaboration), Nature **580**, 339 (2020).
[3] B. Abi *et al.* (DUNE Collaboration), arXiv (2018), 1807.10334 [physics.ins-det].
[4] B. Abi *et al.* (DUNE Collaboration), arXiv (2018), 1807.10327 [physics.ins-det].
[5] B. Abi *et al.* (DUNE Collaboration), arXiv (2018), 1807.10340 [physics.ins-det].
[6] K. Abe *et al.* (Hyper-Kamiokande Collaboration), arXiv (2018), 1805.04163 [physics.ins-det].
[7] M. Antonello *et al.* (MicroBooNE, LAr1-ND, ICARUS-WA104), arXiv (2015), 1503.01520 [physics.ins-det].
[8] F. Tortorici, V. Bellini, and C. Sutera (ICARUS Collaboration), J. Phys. Conf. Ser. **1056**, 012057 (2018).
[9] B. Abi *et al.* (DUNE Collaboration), arXiv (2018), 1807.10334 [physics.ins-det].
[10] B. Abi *et al.* (DUNE Collaboration), arXiv (2020), 2002.03005 [hep-ex].
[11] S. Dolan, U. Mosel, K. Gallmeister, L. Pickering, and S. Bolognesi, Phys. Rev. C **98**, 045502 (2018).
[12] N. Rocco, A. Lovato, and O. Benhar, Phys. Rev. Lett. **116**, 192501 (2016).
[13] N. Rocco, Frontiers in Physics **8**, 116 (2020).
[14] X.-G. Lu, L. Pickering, S. Dolan, G. Barr, D. Coplowe, Y. Uchida, D. Wark, M. O. Wascko, A. Weber, and T. Yuan, Phys. Rev. C **94**, 015503 (2016).
[15] K. Abe *et al.* (T2K Collaboration), Phys. Rev. D **98**, 032003 (2018).
[16] X.-G. Lu *et al.* (MINERvA Collaboration), Phys. Rev. Lett. **121**, 022504 (2018).
[17] T. Cai *et al.* (MINERvA Collaboration), Phys. Rev. D **101**, 092001 (2020).
[18] L. Bathe-Peters, S. Gardiner, and R. Guenette, arXiv (2022), 2201.04664 [hep-ph].
[19] P. Abratenko *et al.* (MicroBooNE Collaboration), Phys. Rev. Lett. **125**, 201803 (2020).
[20] R. Acciarri *et al.* (MicroBooNE Collaboration), J. Instrum. **12**, P02017 (2017).
[21] A. Aguilar-Arevalo *et al.* (MiniBooNE Collaboration), Phys. Rev. D **79**, 072002 (2009).
[22] D. Kaleko, J. Instrum. **8**, C09009 (2013).
[23] R. Acciarri *et al.* (MicroBooNE Collaboration), Eur. Phys. J. C **78**, 82 (2018).
[24] "Table 289: Muons in liquid argon (Ar)," `http://pdg.lbl.gov/2012/AtomicNuclearProperties/MUON_ELOSS_TABLES/muonloss_289.pdf` (2012).
[25] S. K. H. Bichsel, D. E. Groom, "Passage of particles through matter," PDG Chapter 27, Figure 27.1 `http://pdg.lbl.gov/2005/reviews/passagerpp.pdf` (2005).
[26] W. Van De Pontseele, *Search for Electron Neutrino Anomalies with the MicroBooNE Detector*, Ph.D. thesis, Oxford U. (2020).
[27] P. Abratenko *et al.* (MicroBooNE Collaboration), Phys. Rev. D **105**, 112004 (2022).
[28] P. Abratenko *et al.* (MicroBooNE Collaboration), J. High Energ. Phys. **2021**, 153 (2021).
[29] M. Berger, J. Coursey, M. Zucker, and J. Chang, "Stopping powers and ranges for protons and alpha particles," NIST Standard Reference Database 124 (2017).
[30] P. Abratenko *et al.* (MicroBooNE Collaboration), J. Instrum. **12**, P10010 (2017).
[31] C. Adams *et al.* (MicroBooNE Collaboration), Eur. Phys. J. C **79**, 673 (2019).
[32] P. Abratenko *et al.* (MicroBooNE Collaboration), Phys. Rev. Lett. **128**, 151801 (2022).
[33] P. Abratenko *et al.* (MicroBooNE Collaboration), Phys. Rev. D **105**, L051102 (2022).
[34] C. Andreopoulos *et al.*, Nucl. Instrum. Meth. A **614**, 87 (2010).
[35] C. Andreopoulos *et al.*, arXiv (2015), 1510.05494 [hep-ph].
[36] K. Abe *et al.* (T2K Collaboration), Phys. Rev. D **93**, 112012 (2016).
[37] P. Abratenko *et al.* (MicroBooNE Collaboration), Phys. Rev. D **105**, 072001 (2022).
[38] S. Agostinelli *et al.* (GEANT4), Nucl. Instrum. Meth. A **506**, 250 (2003).
[39] R. Pordes and E. Snider, PoS **ICHEP2016**, 182 (2016).
[40] E. Snider and G. Petrillo, J. Phys. Conf. Ser. **898**, 042057 (2017).
[41] A. Bodek and T. Cai, Eur. Phys. J. C **79**, 293 (2019).
[42] W. Tang, X. Li, X. Qian, H. Wei, and C. Zhang, J. Instrum. **12**, P10002–P10002 (2017).
[43] A. Aguilar-Arevalo *et al.* (MiniBooNE Collaboration), Phys. Rev. D **88** (2013), 10.1103/PhysRevD.88.032001.
[44] J. Calcutt, C. Thorpe, K. Mahn, and L. Fields, J. Instrum. **16**, P08042 (2021).
[45] B. Roe, Nucl. Instrum. Meth. A **570**, 159 (2007).
[46] T. Golan, J. Sobczyk, and J. Żmuda, Nucl. Phys. B Proc. Suppl. **229-232**, 499 (2012), Neutrino 2010.
[47] P. Abratenko *et al.* (MicroBooNE Collaboration), Eur. Phys. J. C **82**, 454 (2022).
[48] K. Mahn, *A search for muon neutrino and antineutrino disappearance in the Booster Neutrino Beam*, Ph.D. thesis, Columbia University (2009).
[49] R. Carrasco and E. Oset, Nucl. Phys. A **536**, 445 (1992).
[50] J. Nieves, F. Sanchez, I. Ruiz Simo, and M. Vicente Vacas, Phys. Rev. D **85**, 113008 (2012).
[51] J. Engel, Phys. Rev. C **57**, 2004 (1998).
[52] J. Nieves, J. E. Amaro, and M. Valverde, Phys. Rev. C **70**, 055503 (2004).
[53] J. Schwehr, D. Cherdack, and R. Gran, arXiv (2016), 1601.02038 [hep-ph].
[54] J. A. Nowak (MiniBooNE Collaboration), AIP Conf. Proc. **1189**, 243 (2009).
[55] K. Kuzmin, V. Lyubushkin, and V. Naumov, Phys. Part. Nucl. **35**, S133 (2004).
[56] C. Berger and L. Sehgal, Phys. Rev. D **76**, 113004 (2007).
[57] K. M. Graczyk and J. T. Sobczyk, Phys. Rev. D **77**, 053001 (2008), [Erratum: Phys.Rev.D 79, 079903 (2009)].
[58] C. Berger and L. Sehgal, Phys. Rev. D **79**, 053003 (2009).
[59] D. Ashery, I. Navon, G. Azuelos, H. Walter, H. Pfeiffer, and F. Schleputz, Phys. Rev. C **23**, 2173 (1981).
[60] U. Mosel, Phys. Rev. G **46**, 113001 (2019).
[61] T. Leitner, L. Alvarez-Ruso, and U. Mosel, Phys. Rev. C **73**, 065502 (2006).
[62] T. Sjostrand, S. Mrenna, and P. Z. Skands, J. High Energ. Phys. **05**, 026 (2006).
[63] C. Llewellyn Smith, Phys. Rept. **3**, 261 (1972).

[64] J. Nieves, I. R. Simo, and M. J. V. Vacas, Phys. Rev. C **83**, 045501 (2011).
[65] T. Katori, AIP Conf. Proc. **1663**, 030001 (2015).
[66] D. Rein and L. Sehgal, Annals Phys. **133**, 79 (1981).
[67] S. Mashnik, A. Sierk, K. Gudima, and M. Baznat, J. Phys. Conf. Ser. **41**, 340 (2006).
[68] S. Dolan, G. D. Megias, and S. Bolognesi, Phys. Rev. D **101**, 033003 (2020).
[69] S. Dytman, Y. Hayato, R. Raboanary, J. T. Sobczyk, J. Tena-Vidal, and N. Vololoniaina, Phys. Rev. D **104**, 053006 (2021).
[70] P. Abratenko *et al.* (MicroBooNE Collaboration), Phys. Rev. Lett. **123**, 131801 (2019).
[71] P. Abratenko *et al.* (MicroBooNE Collaboration), Phys. Rev. D **102**, 112013 (2020).
[72] M. B. Avanzini *et al.*, Phys. Rev. D **105**, 092004 (2022).